ANTI-REFLECTIVE STRUCTURED SURFACES ON OPTICAL WINDOWS THROUGH TUNABLE METALLIC ETCH MASKING

by

Benjamin Vaca

A thesis submitted to the faculty of
The University of North Carolina at Charlotte
in partial fulfillment of the requirements
for the degree of Master of Science in
Optical Science and Engineering

Charlotte

2024

Approved by:

Dr. Ishwar Aggarwal

Dr. Thomas Hutchens

Dr. Glenn Boreman

Dr. Susan Trammell

Dr. Tino Hofmann

ABSTRACT

BENJAMIN VACA. Anti-Reflective Structured Surfaces on Optical Windows Through
Tunable Metallic Etch Masking
(Under the direction of DR. ISHWAR AGGARWAL and DR. THOMAS HUTCHENS)

The increasing output power of modern high-energy laser (HEL) systems necessitate robust optical components, particularly in military applications such as directed energy weapons (DEWs), medical procedures, and microfabrication. Traditional anti-reflective (AR) coatings can fail under high-energy conditions due to laser damage and delamination. An alternative solution, anti-reflective structured surfaces (ARSS), utilizes subwavelength features to create a gradient refractive index transition, effectively minimizing Fresnel reflection. Notably, random ARSS (rARSS) fabricated using sputtered discontinuous masking and plasma etching can achieve high laser-induced damage thresholds (LIDT), ten times higher than thin-film AR coatings. Moreover, rARSS is more practical for larger optics and the tunability of the peak spectral performance has been demonstrated by varying parameters in the fabrication process.

This work explores the optimization of metal masking and reactive ion etching (RIE) parameters to enhance ARSS performance, capabilities, and scalability, by correlating fabrication parameters with ARSS feature characteristics and optical transmission. Finally, a “proof-of-concept” demonstration of successful random ARSS on a large diameter and thick optical window was performed and characterized.

Overall, this work lays a foundation for further exploration and development of tunable ARSS, emphasizing scalability for larger optics and diverse substrate materials.

DEDICATION

This thesis is dedicated to…

…my parents and brother, for always being the most incredible support system for every step in my life. I would not have any of the successes I have today without their unconditional love and guidance.

…my girlfriend, Jada, for sticking with me through this long journey. She has been and always will be my motivation.

ACKNOWLEDGEMENTS

First and foremost, I would like to thank my advisors, Dr. Ishwar Aggarwal and Dr. Thomas Hutchens, for their guidance and encouragement over the last few years. Their support has been invaluable, and I am grateful for all the time and energy they have given to me in my time at UNC Charlotte. I would also like to thank my committee members, Dr. Glenn Boreman, Dr. Susan Trammell and Dr. Tino Hofmann for their support and advice. I greatly appreciate all the time my committee has invested in me.

Thank you to the Naval Research Laboratory and the Office of Naval Research, for primary financial support by ONR awards (N00014-22-1-2623) and (N00014-24-1-2138). Also, NSF within the I/UCRC for Metamaterials (2052745) and ONR DURIP for the PlasmaTherm RIE 7000. I am truly grateful and incredibly lucky to have been a part of this research group provided with such generous financial support.

I would also like to thank the Center for Optoelectronics and Optical Communications for the use of its equipment and facilities. Thank you to Dr. Lou Deguzman, Mr. Scott Williams, Mr. Mike Dhooghe, and Mr. Daniel Furr for their patient training sessions and frequent help with equipment issues.

Thank you to the past and present members of the Optical Structured Surfaces Laboratory, Tyler Benge, Jude Yoshino, Tre Genet, Jacob Hay, and Sean Campbell, for all the training, troubleshooting, brainstorming, and general support they’ve given me. I consider myself very lucky to have had such a supportive lab team.

And finally, I’m incredibly grateful to all my friends and family who have been with me throughout my academic career. I’d especially like to thank my girlfriend, Jada,

my parents, Nicki and Oren, my brother Alex, who have all made me the man I am today. I truly could not have made it this far without all the people mentioned here.

TABLE OF CONTENTS

LIST OF TABLES

LIST OF FIGURES

LIST OF ABBREVIATIONS

ABL	airborne laser laboratory
AOI	angle of incidence
AR	anti-reflection
ARSS	anti-reflective structured surfaces
Au	gold
BK7	borosilicate glass
CHF3	trifluoromethane
Cl	chlorine
CVD	chemical vapor deposition
CW	continuous-wave
DEW	directed energy weapon
DC	direct current
DoD	department of defense
DoE	department of energy
DS	double side
DUV	deep ultraviolet
E-beam	electron-beam
F	fluorine
FS	fused silica
HEL	high energy laser
ICP	inductively coupled plasma
LaWS	laser weapon system
LIDT	laser induced damage threshold
LSPR	localized surface plasmon resonance
NIR	near-infrared
ns	nanosecond

NTA	no thermal annealing
O2	oxygen
ODIN	optical dazzling interdictor, navy
PECVD	plasma enhanced chemical vapor deposition
PVD	physical vapor deposition
rARSS	random anti-reflective structured surfaces
RF	radio frequency
RIE	reactive ion etching
RTA	rapid thermal annealing
Sccm	standard cubic centimeter per minute
SEM	scanning electron microscope.
SF6	sulfur hexafluoride
Si	silicon
SiO2	silicon dioxide
SS	single side
TE	transmission enhancement
THEL	tactical high energy laser
UNC	the University of North Carolina
USPL	ultra-short-pulse laser
UV	ultraviolet
VIS	visible

CHAPTER 1: INTRODUCTION

1.1 High Energy Laser (HEL) Systems

The need for optical components to handle a high energy laser (HEL) is crucial in modern laser systems where power level and intensity capabilities are always increasing. For example, directed energy weapons (DEW) within the military such as the Navy's Laser Weapon System (LaWS) (Fig. 1), the Army's Tactical High Energy Laser (THEL), and the Air Force's Airborne Laser Laboratory (ABL) which all have been implemented onto various military defense vehicles or vessels [1]. Aside from the department of energy (DoE) and defense (DoD), there are many commercial applications such as manufacturing, medical procedures, and microfabrication where high purity and high damage resistant optical components are needed. Lasers are also being utilized for treatment of a variety of pathologies within the medical field such as tumor ablation, lithotripsy, dermatology, and a multitude of cosmetic and reconstructive procedures [2].

Figure 1: Applications for high energy laser systems for defense and manufacturing, a) is a 30-kilowatt AN/SEQ-3 laser weapon system (LaWS) aboard a U.S. destroyer (US Navy USS Ponce, 2014), b) is the Optical Dazzling Interdictor, Navy, or ODIN system, and c) a commercial application of HEL systems used for laser cutting.

Understanding the limits of materials used within optical components is extremely important to the performance of the entire system. The purity of the material is a critical parameter for determining the laser induced damage threshold (LIDT) of any material. Impurities within the materials can cause many effects such as absorption loss, scattering loss, and temperature rise which lead to damage to the optics and reduced performance of the system. Impurity defects can cause local hotspots, leading to a rise in thermal stresses, exceeding the melting point and compressive strength of fused silica, leading to severe damage. The impact of these defects on LIDT varies by defect type, size, and location [3].

The main material used for HEL optical components is fused silica because it already has a relatively high laser damage threshold, a broadband transmission and low absorption making it versatile for many wavelengths, low thermal expansion and high durability, and typically high purity which aid in the performance of the optic. Fused silica has a refractive index around 1.5, depending on operating wavelength, and generally has excellent transmission properties, with over 90% transmission within the visible spectrum and high transmission extending into the NIR. The refractive index of fused silica changes with wavelength due to a phenomenon known as dispersion. As the wavelength of light decreases, the energy of the photons increases, leading to a higher refractive index. Conversely, at longer wavelengths, the energy of the photons decreases, leading to a lower refractive index. This wavelength dependence is described by the material's dispersion curve, which for normal dispersion shows that the refractive index gradually increases as the wavelength decreases [4].

1.2 Laser Induced Damage Threshold (LIDT)

All the examples mentioned of HEL systems being implemented into today's world are reliant on the performance of the optical components to ensure desired beam shape, size, and intensity and any damage to these components would be detrimental to the system. Understanding the localized dynamics of laser induced damage can aid in developing strategies for mitigating this damage.

The damage threshold of a material is dependent on many factors such as laser wavelength, pulse duration, and spot size. When a high-intensity laser pulse interacts with an optical component, such as a fused silica window, the material absorbs the energy primarily through nonlinear absorption mechanisms such as multiphoton absorption and avalanche ionization [5]. This absorption excites electrons from the valence band to the conduction band, resulting in the formation of a high-density electron plasma. The excited electrons continue to absorb laser energy and generate free electrons through impact ionization which creates a cascade of increasing electron and plasma density. Increasing the plasma density also increases energy absorption, leading to localized heating within the lattice of the material causing mechanical failure to the surrounding material via thermal expansion shock waves, vaporization and expulsion of material [5].

1.3 Anti-Reflection Techniques

Light incident on a surface boundary between two mediums with different refractive indexes will undergo reflection. Air-glass (n_o = 1.0, n_s= 1.5) interface undergoes reflection of 4% due to this abrupt refractive index shift and can be described by Fresnel equations. Unwanted reflections from transmissive optics can be detrimental in various applications such as high-performance optical lenses, photovoltaic devices, light emitting diodes, and imaging systems. For these applications, reducing reflection is crucial for performance of the system and sometimes even the safety of the surrounding environment [5]. Current anti-reflection technologies involve two major surface treatment techniques to mitigate Fresnel reflectivity, homogeneous and inhomogeneous [6].

It has been demonstrated that discrete multilayer AR coatings can perform very well by taking advantage of interference effects arising from reflections within coatings, however, there still exists material limitations and suffer from laser damage and delamination when used in extremely high energy or power applications [7, 8]. Discrete multilayer AR coatings, which use multiple thin film layers with varying refractive indices, can enhance performance by leveraging interference effects from multiple reflections within the coating layers. However, in extremely high-energy or power applications, these coatings can suffer from laser-induced damage, such as localized heating leading to material degradation, and delamination, where the layers separate due to thermal expansion or mechanical stress. Any impurities present within AR coatings would be detrimental in high power conditions; therefore, it is critical to carefully design and optimize AR coatings for high-power laser applications, considering factors like thermal management, material selection, and coating thickness to minimize the risk of damage.

Homogeneous treatments involve anti-reflective (AR) coatings with multi-layer thin films used to reduce the reflections for a wide range of wavelengths or incident angles. Simple calculation shows that a single homogeneous layer of optical thickness $\lambda/4$ can minimize the reflection of a normal-incident light of wavelength λ, if the coating has refractive index of $n = (n_s * n_o)^{0.5}$, where n_s and n_o represent the refractive index of the substrate and atmosphere, respectively [6].

Theoretically, perfect AR thin film coatings can be very effective as they can suppress Fresnel reflections to nearly zero [10], however, they are limited to applications of low optical fluence (<20J/cm^2 at λ=1064nm for fused silica optics); low radiation (<300kRad Si proton exposure); low environmental variations (temperature and humidity); non-abrasive environments (rain and sand erosion); limited bandwidth; limited incident angle range (<30 degrees); and where the cost of AR coating is not a primary concern [11]. Although materials with a refractive index needed to generate these “perfect” AR coatings do not exist in nature, current specialists utilize multi-layer coatings that expand homogeneous AR coatings to operate for a wide range of transmitting wavelengths and incident angles [9]. These coatings work on the principle of destructive interference, where each layer is engineered so that reflected light waves from different interfaces cancel each other out, reducing overall reflectance. However, their complexity in design and fabrication can increase costs, and they are typically optimized for specific wavelength ranges and angles of incidence. Additionally, these coatings may not perform as well in environments with extreme temperature variations or mechanical stresses, where the different thermal expansions of the layers could lead to degradation over time.

1.4 Anti-Reflective Structured Surfaces (ARSS)

Inhomogeneous surface treatments utilize a gradient refractive index transition instead of the abrupt change seen in polished surfaces, leveraging subwavelength features to eliminate reflections (Fig. 2). Anti-reflective structured surfaces (ARSS), a version of this approach, suppress reflections without the need for multi-layered dielectric or sol-gel coatings. ARSS, as surface relief gratings, transmit only zeroth-order light while higher orders become evanescent, ensuring efficient light transmission with minimal scattering—critical for high optical clarity [12, 13].

These periodic or random metasurfaces rely on nano-scale structures rather than material properties to suppress absorption and reflections. The subwavelength features, typically half the wavelength of operation, create a gradual refractive index transition, akin to the "moth eye" effect [14, 15]. Inspired by natural anti-reflective adaptations in moth eyes, these structures allow smooth light transition from air to the substrate, reducing scattering and enhancing transmission. This effect arises as the glass-to-air volume ratio gradually increases through the ARSS features (Fig. 2).

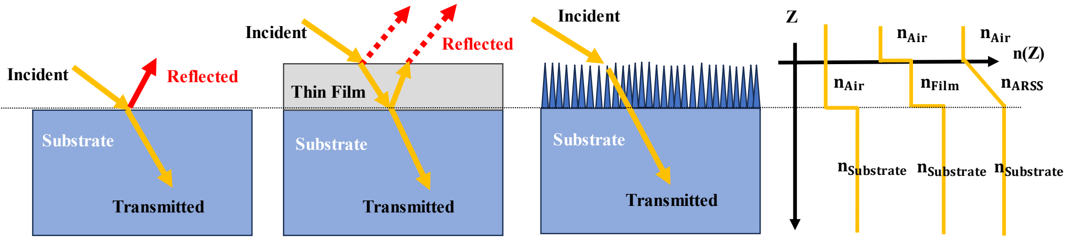

Figure 2: Schematic of a) polished, no coating substrate, b) single layer anti-reflective thin film, compared to the same substrate containing c) ARSS, and d) refractive index profile for each with respect to propagation distance into the material. Appropriate thickness and thin film refractive index are required for reflected waves to destructively interfere. For ARSS, the index shift is gradual for subwavelength feature widths and periodicity therefore all diffraction orders higher than zero become evanescent, propagating only zero order transmission [13].

1.4.1 ARSS via Photolithography Masking

A standard photolithography process, like in the semiconductor wafer industry, can be used to pattern a masking layer onto an optics surface for etching. The process begins with a thin layer of photoresist, a light sensitive material, being applied to the surface via spin coating to create a uniform thick film and a soft baking step to improve adhesion and uniformity. The next step involves aligning a photomask with the substrate. The photomask contains the desired pattern in light and dark regions and is carefully positioned using an alignment tool to ensure accuracy. The aligned substrate and photomask are then exposed to typically ultraviolet (UV) light. The light passes through the transparent regions of the photomask and interacts with the photoresist. If a positive photoresist is used, the exposed regions become more soluble in the developer solution. Conversely, if a negative photoresist is used, the exposed regions become less soluble. After exposure, the substrate is immersed in a developer solution, which dissolves the soluble portions of the photoresist, revealing the pattern on the underlying surface. This is followed by rinsing and drying the substrate. A hard bake may be performed to further harden the remaining photoresist, making it more resistant to the subsequent etching process. The patterned photoresist acts as a mask during etching, where material is removed from the unprotected regions of the optical surface, transferring the pattern from the photoresist to the substrate. Finally, the remaining photoresist is removed using a solvent or plasma etching, leaving the patterned optical surface, which is then inspected to ensure the pattern was correctly transferred and meets the required specifications. This process is widely used to create diffraction gratings.

Tightly packed, periodic subwavelength structures can achieve low reflectance over various wavelengths and be optimized for specific applications. However, ARSS fabrication using photolithography faces challenges such as resolution limits, aspect ratio constraints, and aperture scalability issues, typically limiting patterns to over one micron, which restricts the method largely to infrared applications. Photolithography also struggles with large apertures and non-flat optics, making it suboptimal for fine features or high aspect ratios. Consequently, alternative methods, like random structuring with metal masking, are being explored.

1.4.2 ARSS via Random Masking (rARSS)

Random ARSS (rARSS), on the contrary, is scalable to large and curved optics and can exhibit broadband performance due to subtle variations in feature size and depth. Unlike periodic ARSS, which features regular geometric arrangements like hexagonal patterns, random ARSS has a disordered or quasi-random distribution of nanostructures. Random ARSS are effective over a broader range of wavelengths compared to periodic ARSS, which are usually optimized for specific wavelengths. The smaller and randomly distributed feature sizes formed by rARSS are well suited for visible optics. Fabrication of high-aspect-ratio rARSS features requires a material removal process by plasma etching, with or without the use of an etch mask, where the substrate is etched away to generate structures. This process requires less steps and is less sensitive to manufacturing defects while still maintaining good broadband performance. Studies have shown that while periodic structures can achieve higher peak performance at specific wavelengths, random structures provide more consistent performance across a broader range of wavelengths and angles [11].

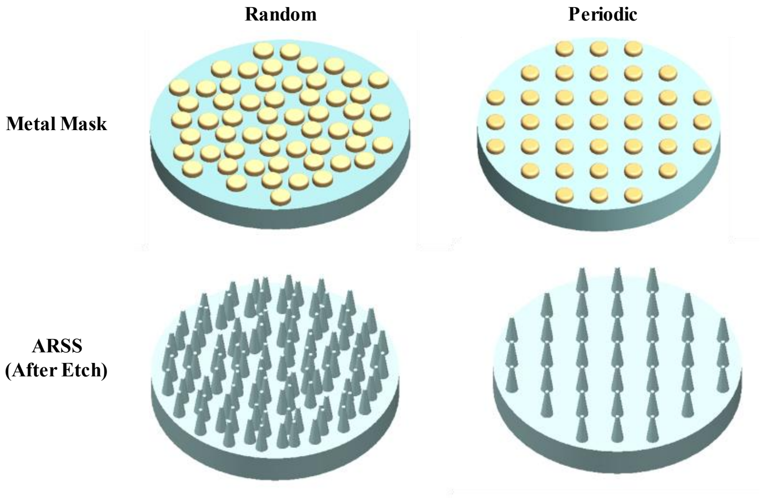

Figure 3: Visual representation of periodic vs random ARSS fabrication. Unlike periodic ARSS, random ARSS (rARSS) has a quasi-random distribution of nanostructures that are effective over a broader wavelength range. Typically, periodic ARSS patterns are limited to over one micron, which restricts the method to infrared applications, whereas rARSS smaller features are well suited for visible optics.

1.5 rARSS Fabrication Methods

1.5.1 Physical Vapor Deposition of Metal Mask

Metal deposition, unlike photolithographic methods, has become an advantageous technique for fabrication of etching masks on large form factor optics [12]. There are many methods of metal deposition available for generating metal thin films onto substrates, however, the main method discussed here involves a physical vapor deposition (PVD) process.

Physical vapor deposition involves using a solid source and a physical mechanism (evaporation or sputtering) to propel target atoms onto a substrate [14]. The two main methods of PVD that will be discussed within this work include electron beam evaporation, and ion sputtering (Fig. 4).

Electron-beam evaporation is a technique that allows for deposition of pure films of materials that have high-melting-point temperatures. It requires a very low vacuum (~10^{-6} to 10^{-8} Torr) to operate but has become one of the most preferred methods of thin film fabrication due to its ability to evaporate virtually all materials at almost any rate [14]. A crucible containing the desired deposited material is placed at the bottom of the vacuum chamber, at the focus of the accelerated electron-beam. A heated filament thermionically emits electrons that are accelerated and focused directly on the material. The energy of the beam will cause the material to melt and evaporate or sublimate, depositing on samples placed in chamber. Controlling the power of the beam, altering the size of the focal spot, and adjusting the scanning range of the beam across the crucible will allow optimization of evaporation conditions and deposition rates [9, 14].

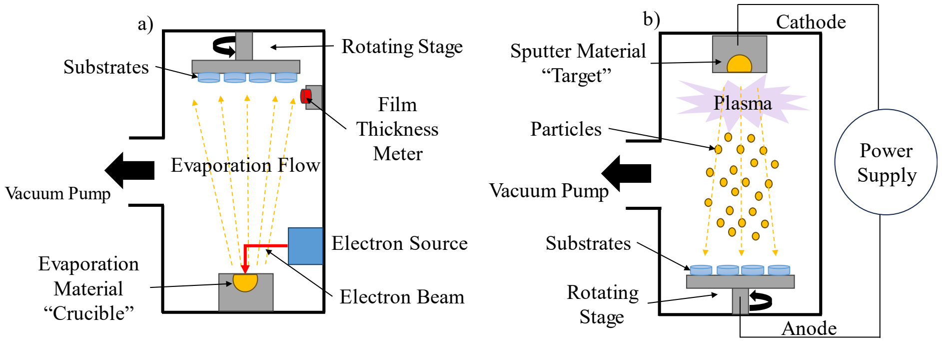

Figure 4: Simplified schematic of the two PVD mechanisms mentioned, a) E-beam evaporation deposition and b) DC sputtering deposition. E-beam evaporation involves a high-energy electron beam heats the target material, causing it to vaporize. The vaporized atoms travel in straight lines in a vacuum and condense on the substrate. The DC sputtering operation creates a plasma that bombards the target material (cathode), ejecting its atoms, that then deposit onto the substrate (anode).

The second PVD technique introduced is sputtering. Here the material that will be deposited (target) is connected to the negative terminal (cathode) within a DC power supply contained within a low vacuum chamber (~10^{-6} Torr). Then the camber is pumped with a non-reactive gas such as Argon to become the medium of plasma discharge. Once the electrode is powered on, plasma forms, and positive ions from the plasma will interact with the target attached to the cathode plate and eject neutral atoms through momentum transfer. These neutral atoms will travel to the positive terminal (anode) where the substrate is held and deposit forming a growing film [9, 14].

rARSS can be fabricated via direct etching of a discontinuous thin film or by generating a random nanoscale metal mask pattern via annealing and dewetting. This approach forms a random, structured pattern on the substrate as metal is etched from select areas. Using this masking approach, tunability of the rARSS features is achieved by controlling the metal mask geometry via dewetting.

1.5.2 Mask Dewetting Technique

Dewetting is a process where a thin film of liquid or solid material retracts from a surface, leading to the formation of droplets or isolated patches instead of a continuous layer. This phenomenon commonly occurs in films that are metastable or unstable on the substrate, such as metals or polymers, particularly when the film's thickness is above a critical threshold. Surfaces that promote dewetting often have low surface energy or are chemically incompatible with the film material. Dewetting can be influenced by factors like temperature, film thickness, and surface roughness, and is often observed in applications involving thin metal films on non-wetting substrates like glass or silicon [15][16].

Dewetting of thin metallic films is a process where a continuous metal layer breaks up into isolated droplets or particles due to instabilities in the film. The process can be initiated by the nucleation of holes in the film, where local thickness variations lead to the formation of voids that grow and eventually cause the film to break apart into discrete islands [17]. The choice of metal for dewetting depends on the desired application and the specific properties needed from the nanoparticles or structures. Each metal exhibits unique dewetting behavior influenced by factors such as surface energy, oxidation resistance, and interaction with the substrate.

A method to increase the size of rARSS to suit infrared optics involves metal deposition and dewetting that generates quasi-periodic islands that act as a metal mask for etching the substrate. This masking method has demonstrated the ability to tune the geometry, height, and periodicity of the etch mask structures through variations in parameters such as deposition thickness and thermal annealing temperature [18, 19]. Dewetting has been shown to be an easy and scalable process for generating a metal etch mask [20, 21].

1.5.3 Etching the Mask Layer into Substrate

Wet and dry etching are two fundamental techniques used in microfabrication, each with distinct characteristics that influence their applications, particularly in isotropic versus anisotropic etching. Wet etching, which is typically used in standard photolithography processes, utilizes liquid chemical solutions to remove material from a substrate, typically in an isotropic manner for amorphous substrates, like fused silica. This isotropic nature can lead to undercutting, where the material beneath the edges of a mask is also removed, limiting it to low aspect ratio features. Wet etching is generally simpler, faster, and more cost-effective, but its lack of directional control limits its use in applications requiring high aspect ratio which is needed for ARSS formation. In contrast, dry etching employs chemical gases or plasmas in a vacuum chamber to remove material, allowing for both isotropic and anisotropic etching (Fig. 5).

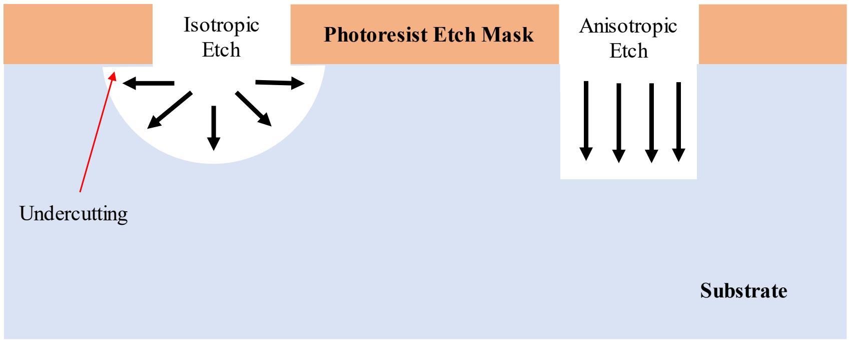

Figure 5: Schematic representation of an isotropic vs anisotropic etching process. Isotropic etching occurs uniformly in all directions, resulting in rounded features and undercutting beneath the mask. Anisotropic etching progresses primarily in one direction (vertically), creating well-defined, straight sidewalls. This method is preferred for high-precision structures and applications requiring accurate pattern transfer.

Anisotropic dry etching, particularly through techniques like reactive ion etching (RIE), etches in the vertical direction, enabling the creation of well-defined, vertical sidewalls with minimal undercutting. This makes dry chemical etching highly suitable for fine control of etching times for fabricating sub-wavelength, high aspect ratio features needed for ARSS.

1.5.4 Reactive Ion Etching (RIE)

Plasma etching involves a combination of physical and chemical reactions of plasma, consisting of partially ionized gas, to remove material from a substrate. This process is one of the major steps needed when manufacturing semiconductor electronic devices and various micro- and nanotechnologies. Typically, a mask is used to guide a desired pattern onto a substrate through the etching process and two major conditions exist for most plasma etching process to be effective: etching must be directional or completed at vertical orientation; and the mask must not suffer any significant design alteration and is etch resistant [22].

Reactive Ion Etching is a specific type of plasma etching that typically requires an evacuated chamber utilizing a radio frequency (RF) power supply and a reactive gas, or a mix of multiple gases. In an evacuated chamber, plasma is ignited when the RF power supply is applied. The substrate being etched is placed on the bottom cathode electrode so that when plasma strikes, electrons are ripped away from the gas molecules, causing collisions with other gas molecules, generating a mixture of neutral molecules (radicals), positive ions in plasma, and electrons that will react with the walls of the chamber as well as the substrate. The interaction at the substrate consists of a voltage difference generated by the electrodes and will result in an electric field perpendicular to the substrate surface. This electric field generated by the voltage difference between the plasma and the substrate accelerates positive ions towards the sample and is the driving mechanism for the directionality of the etching process.

Once positive ions accelerate towards the substrate, they bombard the surface, transferring energy to neutral radicals and causing material to sputter or disperse, a process known as ion-induced etching. The byproducts of this etching process must be volatile enough to be removed from the surface; otherwise, they can redeposit and compromise the uniformity and precision of the etch. Ensuring the production and removal of volatile byproducts is a key factor in achieving high-quality etching results, especially for complex or high-aspect-ratio structures.

Different gas reacts differently with specific materials therefore the plasma gas must be selected based on the substrate to be etched. Substrates consisting of silicon react best with fluorine or chlorine-based gasses such as sulfur hexafluoride (SF6), octafluorocyclobutane (C_4F_8), trifluoromethane (CHF_3), or boron trichloride (BCl_3), typically oxygen (O_2) mixed in as well to oxidize surface layers and aid in material removal [9, 22, 23].

For example, the reaction between SiO_2 and SF_6 in a plasma etching environment can produce volatile silicon tetrafluoride (SiF_4), along with sulfur dioxide (SO_2) and other byproducts depending on conditions. The reaction generally proceeds as follows:

$$SiO_2 + SF_6 \rightarrow SiF_4 + SO_2 \qquad (1)$$

In a plasma environment, SF_6 dissociates to produce reactive fluorine (F) species that interact with SiO_2, facilitating the etching process by forming volatile SiF_4. This reaction may also produce additional byproducts if other gases or contaminants are present.

Adjustments in etching parameters, such as temperature and gas composition, are often made to enhance the volatility of byproducts, facilitating their effective removal and preventing redeposition. Factors to achieve precise material removal include chamber pressure, bias power, gas composition and flow rate, substrate temperature, and etching time are critical in controlling etching efficiency and ensuring that volatile byproducts are effectively evacuated [22].

The plasma etching tool that was used for etching within this work was a PlasmaTherm 7000 plasma etching machine (Fig. 6). This machine can control chamber pressure, bias power, has various available gasses (Ar, $\mathrm{CHF_3}$, $\mathrm{SF_6}$, and $\mathrm{O_2}$), and can hold up to 12-inch diameter substrates.

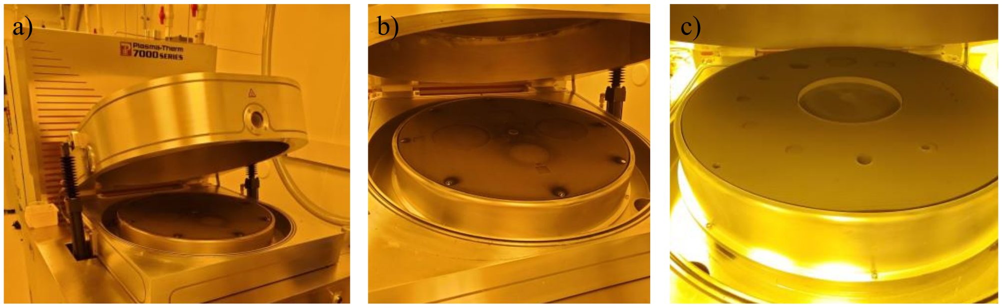

Figure 6: PlasmaTherm 7000, loaded with b), a small one-inch diameter substrate and c), a large eight-inch diameter substrate. This machine can control chamber pressure, bias power and has various available gasses for plasma ignition (Ar, CHF_3, SF_6, and O_2). Adjustments to the graphite platen were designed to accommodate larger windows.

In rARSS fabrication, the directionality of plasma relative to the substrate plays a crucial role in achieving precise nano-structure patterns. The metal mask, often made from materials like gold, acts as a resistive layer that regulates the depth of the etch by selectively shielding certain areas of the substrate. This selective etching is essential for creating the desired nano-array patterns, as the mask's resistance controls which regions of the substrate are exposed to plasma.

1.6 Previous Work in rARSS

Commercial groups like TelAztec and Nanohmics are commercial examples of developing anti-reflective structured surfaces for a variety of optical applications. TelAztec, for instance, specializes in the fabrication of moth-eye ARSS that utilize interference lithographic techniques to produce nanoscale structures on various substrates, including glass, silicon, and polymers, making their technology suitable for use in solar panels, optical sensors, and military optics [24]. TelAztec's capabilities include producing large-area ARSS with high uniformity and durability. Nanohmics, on the other hand, focuses on creating ARSS through more scalable and cost-effective methods. Their approach allows production of ARSS on flexible substrates, which is particularly advantageous for integrating anti-reflective properties into wearable devices and flexible displays [25]. However, while commercial companies like TelAztec and Nanohmics' techniques offer ARSS, there still exist many limitations for extremely high-power applications requiring anti-reflection.

Groups at UNC Charlotte led by Dr. Aggarwal, Dr. Poutous, and Dr. Hutchens have been studying ARSS for over a decade. Primary efforts have involved fused silica, gold masking, and laser induced damage threshold testing. Random anti-reflection structured surfaces (rARSS) were created on fused silica substrates using a three-step process: gold deposition, rapid thermal annealing (RTA) to form random island masks, and reactive ion etching (RIE).

Previous results indicate that increasing bias power during etching shifts the sample’s peak transmission wavelength toward the infrared (Fig. 7) [9], leading to etch processes for specific wavelength targets. In this thesis, the focus is on refining rARSS recipes for the UV to NIR range (200–1000 nm), therefore a bias power of 500 W was used for further recipe tuning.

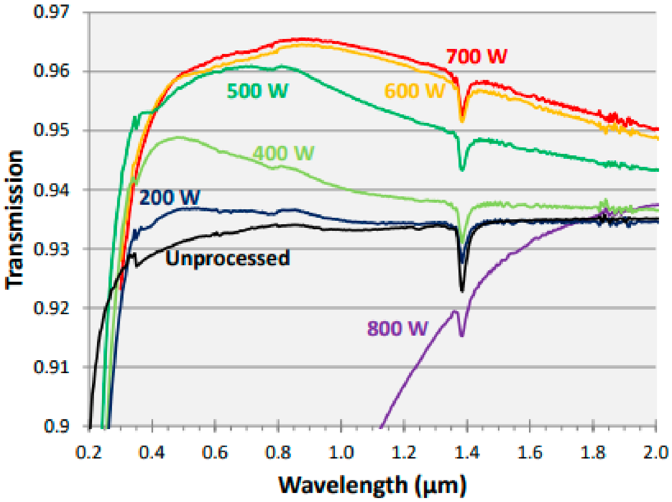

Figure 7: Measured spectral transmission for an unprocessed polished fused silica substrate (black) compared to fused silica substrate processed with rARSS on a single side. Bias power was increased for each sample and measurement was completed at normal incidence. This data was taken from Ref. [9].

Also, investigations into how a fixed Au deposition thickness responds to changes in RTA temperature were completed by monitoring depth, surface roughness, and lateral feature size distributions of the Au mask before etching. Results show that adjusting RTA temperature allows control over the metal mask features: as temperature increased, gold mask features grew larger and more isolated (Fig. 9), resulting in varied etched feature sizes and shifts in scattering wavelength (Fig. 8).

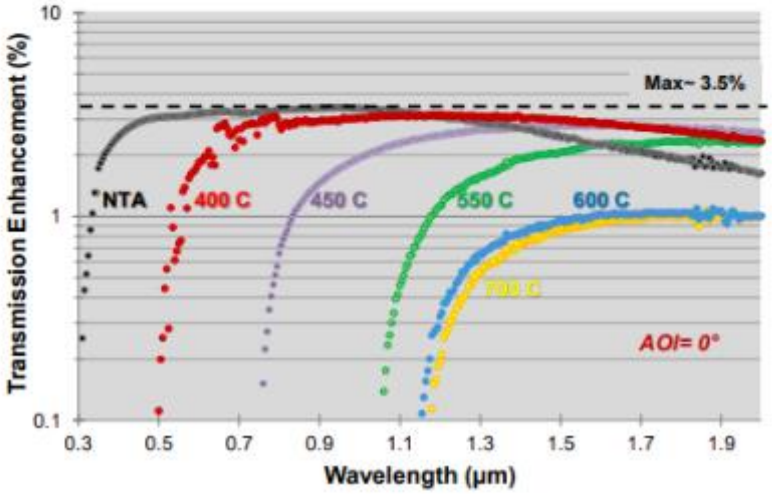

Figure 8: Measured spectral transmission enhancement for fused silica substrate with rARSS fabricated on a single side. Six samples were tested with baseline representing a substrate with metal deposition but no rapid thermal annealing (NTA), and the other 5 samples annealed at increasing temperatures. Measurements were taken at normal incidence. The vertical scale is logarithmic, and the black dashed line indicates the maximum possible transmission enhancement for ARSS on a single side of substrate, which is equal to the maximum value of Fresnel losses per fused silica surface. This data was taken from Ref. [9].

Figure 9 shows SEM images taken for each of the RTA temperatures tested. The top row shows each sample following Au deposition and RTA, while the bottom row displays the resulting ARSS for each metal mask after an identical RIE process. Looking at the Au samples, “voids” (dark areas in the Au film) are formed at baseline, 400 °C, 450 °C, and 550 °C, with the void size progressively increasing with higher annealing temperatures. However, at 600 °C and 700 °C, these voids become so large that only isolated gold islands remain. In the fused silica samples post-etching, a similar pattern is evident, with the etched voids enlarging to form sizable craters, where low fill factor led to flat spots and no transmission enhancement [9].

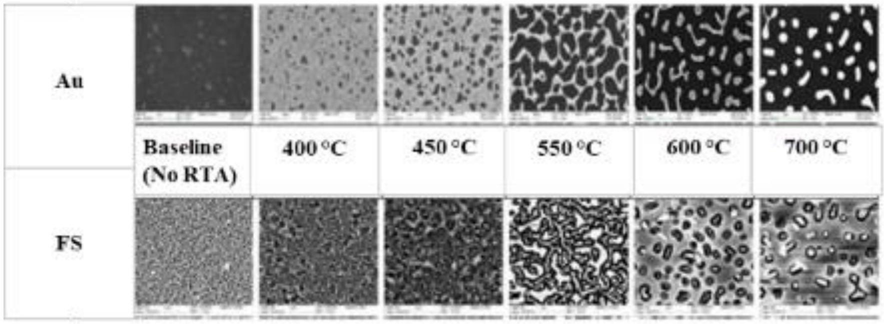

Figure 9: Scanning electron micrographs of previously tested fused silica samples. The top row shows gold (Au) features produced after Au sputtering (~20 nm for all) and RTA. The bottom row shows the features formed on the fused silica substrate after etching. Images were taken at 20,000x magnification. This figure was adapted from Ref. [9].

Building on these results, I developed a plan to refine and tune this process for generating Au metal mask features for deposition thicknesses below 20 nm. Again, within the scope of transmission enhancement within the 200–1000 nm wavelength range. My goal is to create a detailed database linking metal mask and RIE processing parameters to specific ARSS performance for future reference and further scalability of the process. Initial Au deposition thickness in this previous work targeted MWIR ranges, however, I will focus on the VIS to NIR, and optical mask verification methods as they apply to larger samples.

Other previous work involves testing the durability of double-sided random anti-reflective structured surfaces (rARSS) under high-power near-infrared continuous-wave (CW), nanosecond (ns), and ultra-short-pulse laser (USPL) irradiation. The LIDT of

ARSS on fused silica has been shown to be 10 times that of thin-film AR and approaches the LIDT of the bulk material for ns pulse regime [27], and USPL [28].

No visible damage was observed on optical windows or rARSS-treated surfaces for up to 2 kW of CW laser power or an intensity of 70 MW/cm² for a duration of 1 hour [26]. Thermal data indicated only slight heating in rARSS-treated samples under normal operating conditions compared to untreated samples. This heating was evenly distributed, with a minor hot spot at the laser/substrate interface, but well below fused silica's melting point, posing no immediate risk of damage. Additionally, no drop in power throughput was detected, suggesting the Laser-Induced Damage Threshold (LIDT) was not reached for continuous wave (CW) exposure, even though temperatures increased slightly. Thermal monitoring indicated only a slight temperature rise, confirming the rARSS's robustness for extended laser exposure with no adverse effects or power throughput loss [26].

LIDT probability was also assessed for entrance, exit, and simultaneous entrance/exit surface damage using a 1064-nm wavelength laser with 7 ± 1 nanosecond pulses [26]. The rARSS-treated surfaces were optimized for antireflective performance at 1064 nm, achieving a 3.2% increase in transmittance (Fig. 10). Damage onset was observed between 90–100 J/cm², with a 100% probability of damage at 200 J/cm², marking bulk material damage initiation (Fig. 10) [27]. Entrance-side damage showed localized melting and reflow without fractures, indicating a thermal effect, while exit-side damage exhibited a ballistic nature with crater formation and fracturing, indicating a breakdown mechanism.

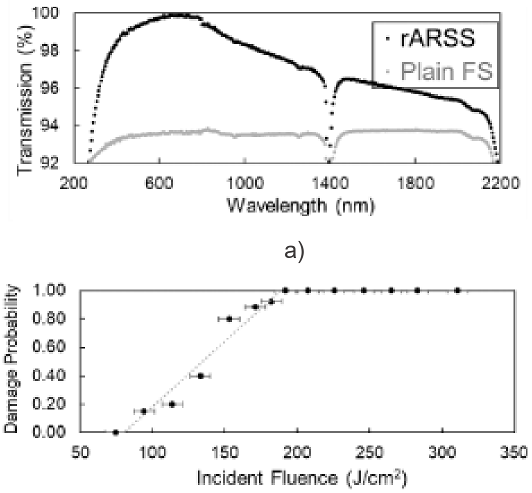

a)

b)

Figure 10: Measured broadband spectral transmission, a), and laser damage threshold, b), for rARSS processed fused silica compared to a plain unprocessed fused silica substrate. Broadband transmission enhancement and increased LIDT is achieved through rARSS processing. This data was taken from Ref. [27].

Previous results showed high LIDT for rARSS under nanosecond pulses, but testing to femtosecond pulses was also done to assess rARSS performance under extreme, non-thermal conditions [28]. Under ultrashort pulse (sub-picosecond) laser irradiation, non-thermal damage due to multiphoton absorption and nonlinear ionization occurs. Z-scan measurements on silica samples with and without ARSS under femtosecond laser irradiation showed similar nonlinear absorption behavior and damage thresholds, with both samples exhibiting irreversible changes in transmission at a maximum peak intensity of 34.8 x 10^{12} W/cm^2 [28]. Confocal microscopy revealed two damage types: at lower intensities, refractive index changes appeared as small bright spots within the sample, while at higher intensities, surface ablation created depressions of 10–20 µm depth and approximately 50 µm in diameter (Fig. 11). The ablation was smoother on the ARSS-treated surface than on the polished silica, suggesting ARSS does not increase damage risk, supporting its use as a durable alternative to AR coatings in femtosecond laser systems [28].

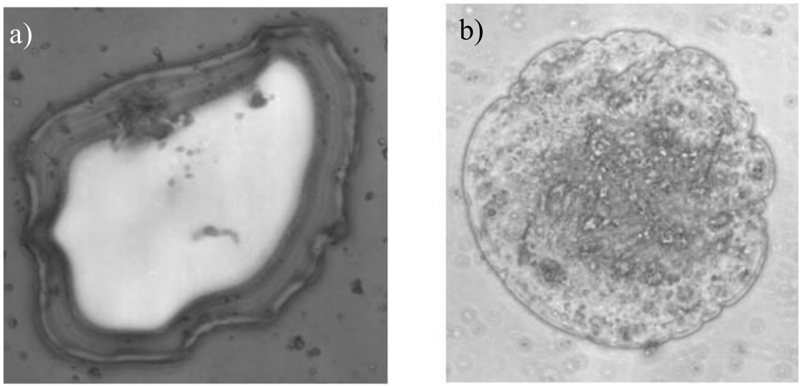

Figure 11: Confocal microscope images of ablated damage spot on a) silica sample with ARSS, where the bright area was smooth and b) a polished silica sample, where the damaged area was rough. These images were taken from Ref. [28]

1.7 Thesis Overview – Tunability of ARSS Features and Performance

Anti-reflective structured surfaces (ARSS) have become a key focus for research within companies like TelAztec and Nanohmics, as well as many academic environments where they are advancing commercial applications of anti-reflective technology, particularly due to LIDT as just shown in section 1.6.

I plan to expand this research by further exploring the parameters within the fabrication process already established and tuning the recipe to control the transmitting capabilities of optics. Controlling ARSS performance can be achieved by adjusting the metal mask features through variations in fabrication parameters such as deposition thickness and annealing temperature. The ability to control the peak transmitting wavelength while maintaining broadband transmission enhancement has been shown within this work.

By studying the masking in Chapter 2 and plasma etching in Chapter 3, a large database of optimal parameters for high-performance ARSS fabrication, that can be referenced for future studies and manufacturing, was generated. The tuning of these recipes in Chapters 2 and 3 was performed on 1-inch diameter fused silica witness samples, however, Chapter 4 demonstrates the successful scaling of these recipes to a larger 8-inch diameter by 1.5-inch thick JGS2 fused silica window. Exploring the uniformity and consistency of these methods is crucial for scaling up the process to larger optics consisting of a wide range of substrates. The ARSS recipe targeted peak transmission enhancement around 600 nm, achieving ~3% transmission improvement with single-side processing (Fig. 12). Adjustments to the equipment and processing parameters were needed for scaling these ARSS recipes. Details of this will be discussed in Chapter 4.

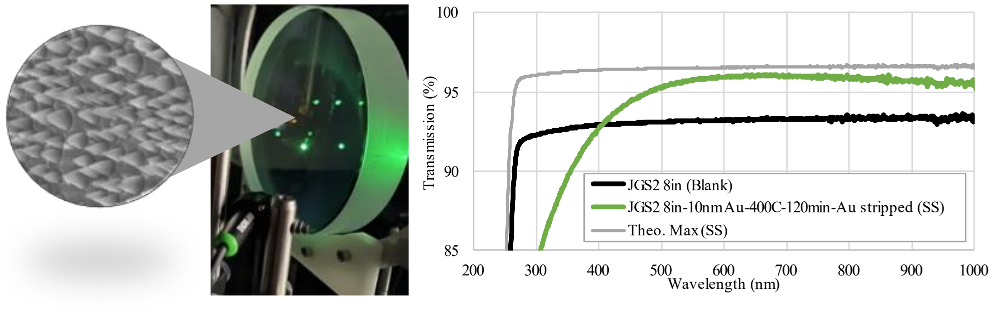

Figure 12: Measured spectral transmission for 8-inch diameter by 2-inch thick JGS2 fused silica substrate for single side ARSS fabrication (green) compared to that of a blank unprocessed window (black) and a single side ARSS theoretical maximum (gray). The ARSS recipe is designed to target a peak enhancement of around 600 nm, achieving ~3% improvement for single side processing, ~97% of theoretical maximum.

CHAPTER 2: FABRICATION METHODS AND TUNABILITY OF ARSS THROUGH CONTROL OF METAL ETCH MASK

2.1 Introduction to ARSS Fabrication via Metallic Etch Masking

This chapter demonstrates how to control the submicron-scale unit structure of ARSS features which drives transmission enhancement. A scalable fabrication method for controlling the unit structure and periodicity was explored, with waveband tunability achieved through control of the metal masking step, shown later in Chapter 3.

The top-down ARSS fabrication method on fused silica involves thin film deposition, dewetting, and etching the mask pattern into the substrate (Fig. 13). Metal mask features can be controlled by adjusting deposition thickness and annealing temperature, directly correlating to the optical performance and transmission spectra of the ARSS after etching.

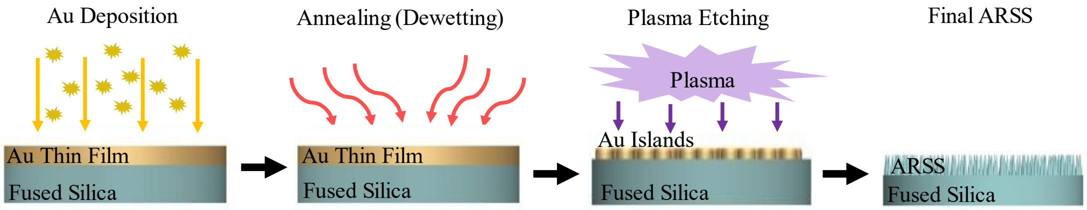

Figure 13: Visual schematic of each step within the ARSS fabrication process. The first step consists of metal deposition, Au for this scenario; step two involves annealing to initiate the dewetting and produce Au islands; the final step requires a plasma etching process that will selectively etch the substrate based on the geometry of the metal mask, leaving behind high aspect ratio ARSS features.

Fused silica (FS) and gold (Au) were chosen as the substrate and deposited metal etch mask, respectively. FS or silicon dioxide (SiO_2) is used for a very large range of optical applications and Au has favorable surface tension and nanoparticle size. Additionally, gold's inherent resistance to oxidation enables diverse optical applications [19]. For masking studies, 1-inch-diameter, 0.0625-inch-thick and 1-inch-diameter, 0.059-inch-thick double-side polished silica windows (Quartz Plus, Inc., Brookline, NH, USA and ESCO Optics, Inc., Oak Ridge, NJ, USA) were the primary substrates used. Corning 7980 is an ultraviolet (UV) grade FS with very low absorption around the visible spectrum.

2.1.1 Fabrication Methods

Au was deposited using a direct-current (DC) sputter deposition system (ACT 1800-F, AJA International, Inc., Hingham, MA, USA) on a rotating stage. For this study it was important to ensure a repeatable process for all the depositions by maintaining the chamber pressure, gas levels, and power levels while having the ability to vary and control the deposition thickness by correlating thicknesses to deposition time, or sputter time. The target used was gold (Au), the substrate was fused silica (FS), and the gas for plasma discharge was argon (Ar). The target connects to the cathode of the DC power supply while the substrate is connected to the anode. Once power is applied to the system, a plasma containing positive Ar ions is formed and will interact with the target, ejecting neutral Au atoms to travel to the anode and deposit on the substrate. Au was deposited with various nominal thicknesses ranging from 5-15 nm on single as-polished side of the silica substrates.

After deposition thicknesses were established, an annealing step was performed at various temperatures to generate different metallic masks with unique features. Heat applied to these thin film layers initiates the dewetting process as the gold nanoparticles deposited on the substrate bond together to form Au nanoparticle “clusters” that accumulate into islands. Temperatures of 300-500 °C were tested, while never fully reaching the Au bulk melting temperature of 1064 °C [13]. Annealing was performed within a 3/12 muffle furnace, (Nabertherm GmbH, Lilienthal, Germany). A ramping time of ~15 minutes to reach peak temperature setting was used, then held for 10 minutes. The samples were then cooled down until safe to handle.

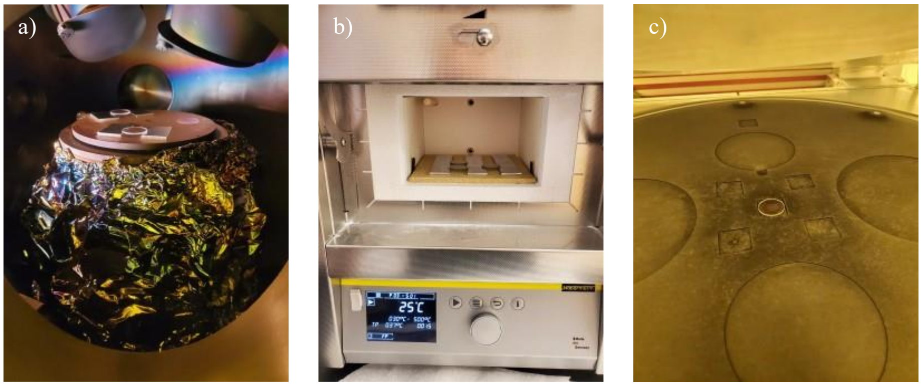

Figure 14: Test substrates within each of the equipment used for fabrication steps, a) is the AJA sputtering machine for metal deposition, b) is the Nabertherm Furnace for annealing, and c) is the PlasmaTherm7000 for direct plasma etching.

Once the desired Au mask is generated, the pattern can be etched into the silica substrate via fluorine-based reactive ion etching. Transfer of these Au masks by etching to form ARSS is discussed in Chapter 3.

2.1.2 Analysis Methods

A comprehensive database of masking layer fabrication methods and resultant surface feature dimensions collected by scanning electron microscopy (150 SEM, Raith GmbH, Dortmund, Germany) as well as transmission spectra from wavelengths 200-1100 nm (CARY 60, Agilent Technologies, Inc., Santa Clara, CA, USA) were collected to track and analyze the Au dewetting process.

SEM is ideal for imaging these metal masks due to its high resolution for nanometer-scale features. However, challenges arise when imaging continuous versus discontinuous films. Continuous films allow better electron conduction, reducing charging effects, while discontinuous features like isolated nanoparticles or dewetted islands cause significant charging, leading to image distortion. Metals' high reflectivity can also result in backscattering, creating bright, overexposed areas in the image. Because of this, careful attention to the electron acceleration voltage was needed.

The SEM images, adjusted to 500 x 1000 pixels, taken at 50,000 times magnification were first imported into MATLAB (MathWorks, Inc., Natick, MA, USA). The MATLAB Image Thresholder and Image Region Analyzer applications were used to convert the SEM grayscale image into a binary image. The binary image was used to determine three characteristics: fill factor, a measure of how much of the surface is covered by the masking material, average island equivalent diameter, and the island separation distance, or periodicity.

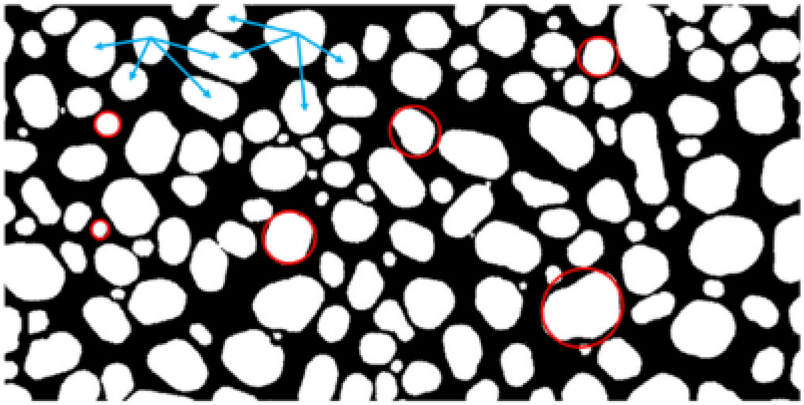

Figure 15: Binarized SEM image of one of the Au masks. The average separation distance is measured from centroids of surrounding islands, indicated by the blue arrows. The average equivalent diameter is measured by referencing the area of the island to a circle with the same area, indicated by the red circles, that diameter is taken as the equivalent diameter. All measurements were measured in pixels and converted to nm using the scalebars within the SEM image footer.

The fill factor was determined by calculating the total number of pixels that were over the threshold during binarization and dividing by the total number of pixels in the image. Equivalent diameter was determined utilizing the MATLAB Image Region Analyzer application. The island segmentation was performed with 8-connectivity, “regionprops” function, so that any two adjacent pixels are considered part of one island. The number of connected pixels for each island, excluding islands of around 10 pixels or less, and an area calculation consisting of the number of pixels in each region was also listed. The equivalent diameter (in pixels) was then determined based on the diameter of a circle with the same area (number of pixels) as the region of interest, calculated by rearranging the area equation for a circle.

To determine the island periodicity, the centroid of each island on the new list was calculated and cataloged as a point on the x-y plane. Then for each point, the distance to the nearest other centroid was found and listed. Both the average and the standard deviation of these distances were scaled and used as a radius for the following step. For each centroid, the distance to all neighboring centroids within the radius was found, averaged, and listed. The average of these averages was taken to be the island periodicity. The periodicity was taken as the average Euclidian distance between each island and its neighbors, averaged over all islands. Where n is the total number of islands, and m is the islands whose centroid is within a radius for each n.

$$\frac{1}{n}\sum_{i=1}^{n}\frac{1}{m}\sum_{j=i}^{m}\sqrt{\left(x_i - x_j\right)^2 + \left(y_i - y_j\right)^2} \qquad (2)$$

All analysis was initially calculated in pixels and converted to nm based on the scale bars present within the SEM images. The conversion was determined to be ~2.22 nm per pixel at 50,000x magnification.

ARSS feature measurements were done with this same method of SEM analysis as well as additional measurements with an Olympus LEXT UV-confocal microscope. The confocal measurement yields the vertical distance (depth) between the highest peak and the lowest valley present on the surface of the substrate allowing for further characterization of ARSS formation.

2.1.3 Theoretical Models

To fully understand the nano-scale unit structure dependency on the transmission capabilities of fused silica optics, simulation models using Ansys Lumerical modeling software (Fig. 16, Table 1) were completed. Several key trends were tested to reinforce the theory of ARSS functionality and demonstrate the ability to tune and control the performance of optics based on the geometry of the structures As the geometry of these structures is modified, such as by adjusting the height, width, or spacing of features, the effective refractive index can be finely tuned, which in turn enhances anti-reflective properties across a broad wavelength range.

A series of models were generated to explore the relationship between the nanoscale unit structure and the transmitting wavelength in ARSS. Five models were created for ARSS on fused silica substrates, each utilizing cone-shaped pillars as geometric reference. These pillars maintained consistent dimensions for the bottom and top radii, measuring 75 nm and 60 nm respectively, with a fixed periodicity of 190 nm. However, the feature height was systematically increased across the models to observe its impact. The results clearly demonstrated a shift in the transmission peak towards higher wavelengths as the pillar height increased (Fig. 16). This trend highlights the strong dependency of wavelength transmission on the vertical geometry of the nanostructures, underscoring the potential for tuning optical properties through precise structural modifications.

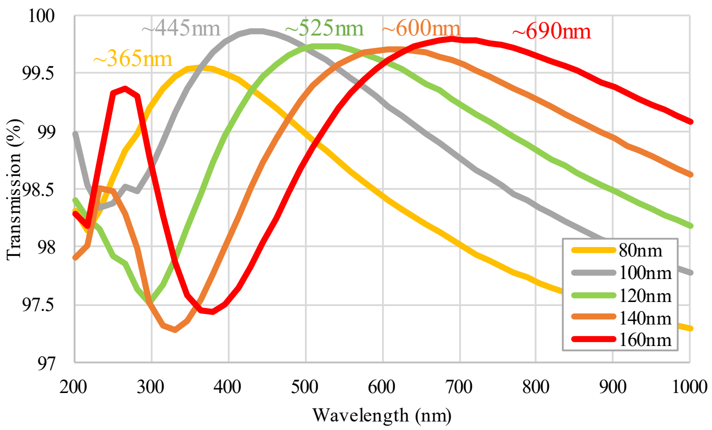

Figure 16: Simulated transmission spectra for an ARSS model with pillar arrays of 75 nm bottom radius, 60 nm top radius, 190 nm periodicity, and varying heights. Increasing pillar height shifted the transmission peak to higher wavelengths, indicating that peak transmission wavelength depends on ARSS feature height. This data was simulated using Ansys Lumerical.

Another series of models were designed to investigate the impact of altering both the size and periodicity of nanostructures on the transmission properties of the optic. In this study, the dimensions and spacing of the cone-shaped structures on the fused silica substrate were systematically increased in steps. As shown in Table 1, the transmission efficiency and peak transmitting wavelength both exhibited a clear upward trend as the size and periodicity of the structures increased. For example, Model A with a height of 30 nm and a periodicity of 50 nm achieves a peak wavelength of 250 nm. In contrast, Model F, with a height of 160 nm and a periodicity of 210 nm, has a peak wavelength of 706 nm. This indicates that by increasing the feature dimensions and periodic spacing, it is possible to enhance both the overall transmission, and the range of wavelengths transmitted, further confirming the tunability of optical properties through structural design adjustments.

Table 1: ARSS geometry and periodicity model results

Model Label	Radii (top, bottom) (nm)	Height (nm)	Periodicity (nm)	Transmission (%)	Peak Wavelength (nm)
A	10, 15	30	50	97.1	250
B	20, 25	50	75	98.1	265
C	30, 37.5	75	112.5	98.8	347
D	45, 56.25	112.5	168.75	99.3	461
E	60, 75	140	190	99.6	608
F	70, 85	160	210	99.8	706

The models demonstrate that the nanoscale unit structure plays a critical role in controlling the peak transmission wavelength, offering insights into optimizing optical performance through precise masking techniques, which will be demonstrated within this work.

2.1.4 Summary of rARSS Fabrication via Metallic Etch Masking

This chapter explores the role of submicron-scale unit structures, and periodicities, in driving transmission enhancement through the fabrication of Anti-Reflective Structured Surfaces (ARSS). A top-down fabrication method was developed, focusing on controlling the periodicity and structure of these unit features, which was demonstrated to enhance transmission across specific wavebands. The fabrication process begins with metal masking using thin-film deposition and thermal dewetting, with Au as the metal and polished fused silica (FS) as the substrate. By varying the deposition thickness, annealing temperature, and the metal used, precise control over the mask geometry is achieved. This mask geometry, in turn, directly influences the transmission spectra and optical performance of the ARSS after etching. Specifically, the periodicity and fill factor of the mask features governs the waveband tunability, dictating where transmission peaks occur. Gold's favorable surface properties, including its resistance to oxidation, further support its use in this process. The Au mask is then transferred onto the silica substrate via reactive ion etching, as detailed in Chapter 3.

2.2 Tunability of Metal Mask Features

Transmission data and SEM images were collected at each processing step, creating a comprehensive database for characterization of the blank substrate, metal thin films of various thicknesses, and metal masks after dewetting. Au was deposited with various nominal thicknesses, 5, 10, and 15 nm, on a single side of the silica substrates. CARY spectrometer was used to measure the transmission spectra for 200-1100 nm range. Annealing was performed at various peak temperatures from 300 to 500 °C. A ramping time of ~15 minutes to reach peak temperature setting was used, then held for 10 minutes. The sample was cooled down until it was safe to handle.

Recently, a method for repetitive deposition and dewetting has been shown to allow for even broader tunability of the ARSS etch mask [9, 13, 18]. “Rounds” of repeated deposition and annealing were performed with same settings as “seed” step or Round 1. The initial thickness before the first annealing will set the feature periodicity and additional steps of deposition and annealing will increase the size of the islands already present or “seeded”. This increase in feature size allows for deeper etch depths translating to taller features, extending the gradual index change to perform AR at longer wavelengths. A diagram for how this repetitive masking process is done and where measurements for characterization were completed is shown in Figure 17, where details for masking large and small substrates are presented.

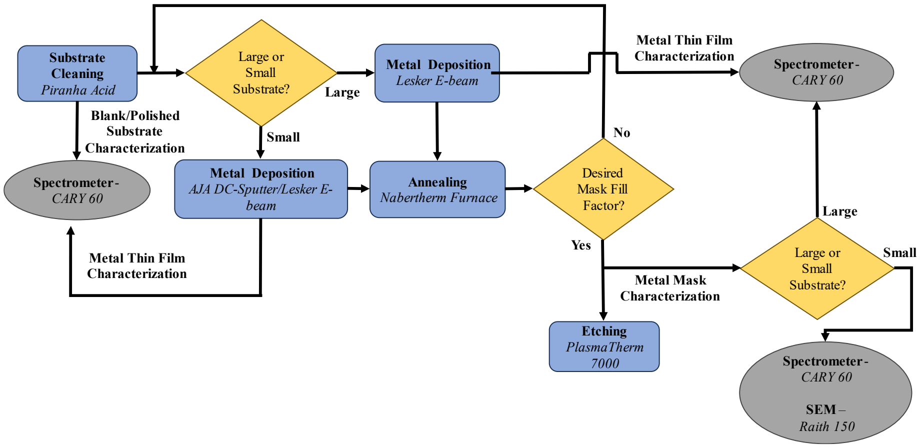

Figure 17: A step-by-step ARSS fabrication diagram via metal masking, with spectrometer measurements and SEM images at each stage on small substrates to ensure repeatability for larger substrates without SEM access. Transmission spectra characterization enables correlating SEM features on small substrates to those on large substrates that are too big for imaging.

The purpose of explaining this process for both small and large optics is to show that experimental results from the fabrication of Au features on smaller optics can be transferred to large scale optics where invasive imaging/analysis of metasurface features are not readily available. By characterizing each step of fabrication, we can correlate the SEM images and transmission spectra produced from these small optic samples to verify masking on larger optics with consistency and confidence.

2.2.1 Control of Metal Mask Features with Deposition Thickness and Annealing Temperature

Exploring different combinations of deposition thickness and annealing temperatures allowed generation of a broad range of masks that could all translate to specific capabilities. The primary substrate chosen for this study was 1-inch-diameter, 0.0625-inch-thick double-sided polished corning 7980 fused silica windows (Quartz Plus, Inc., Brookline, NH, USA). This mask formation is directly dependent on the thickness of the thin layer of Au deposited as well as the temperature of annealing. For thicker Au layers (10-15 nm), higher temperatures (400-500 °C) were needed to fully complete the dewetting process and produce islands.

As seen in previous research [9], a clear shift in the size and periodicity established for each combination as well as a dependency for efficiency of forming the Au islands through the dewetting process is seen. It is apparent that increasing deposition thickness and annealing temperature also results in an increase in size and relative spacing for the Au islands formed on the substrate. This is clearly seen visually within the SEM images (Fig. 18) for each of the combinations tested.

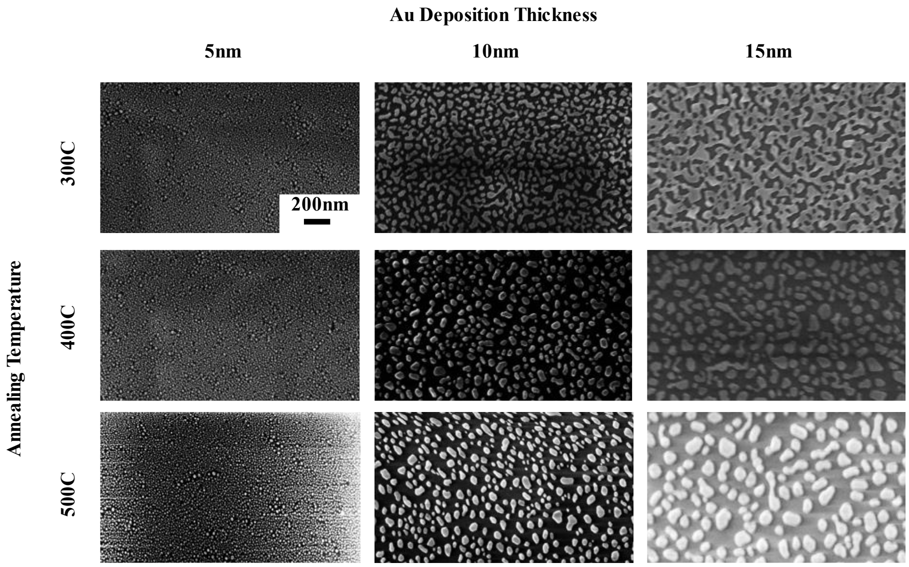

Figure 18: SEM images for metal masks consisting of three Au deposition thicknesses (5, 10, and 15nm) annealed at three temperatures (300, 400, 500 °C). The images are of the same scale and were taken at 50,000x magnification in the center of the substrate.

A correlation between annealing temperature and the ability for the dewetting process to successfully generate island structures on the substrate was also seen. For ~15nm deposition thickness, annealing must be completed at temperatures above 400 °C to generate an array of separate Au features. The sample annealed at 300 °C shows a continuous flow of Au on the surface with periodic holes implying dewetting was partially completed. Whereas higher annealing temperatures (>400 °C) sufficiently melted most of the Au bonds on the substrate and reformed into Au nanoparticles, accumulating into resolvable islands. Looking at the same deposition thickness of 15nm, annealing at 400 °C generates partially formed islands having a larger range of feature dimensions with an average equivalent diameter and periodicity of 72 nm and 133 nm, respectively. Annealing at 500 °C generated similar, yet much more uniform structures having an average area and periodicity of 101 nm and 178 nm, respectively. Comparing these results to the previous work (Fig. 9), we see the dependency of initial thickness on the island formation. Reducing the initial deposition thickness lowers the temperature required for dewetting, as less Au is present on the surface, influencing island formation. Increasing the average size and periodicity is a direct result of the uniformity of the islands and efficiency of the dewetting process at correct temperatures relative to the deposition thickness.

The optical transmission spectra for samples containing ~15nm deposition thicknesses with and without annealing shows a definite correlation from the formation of islands to the resulting transmission (Fig. 19). Annealing at 300 °C, the Au film undergoes partial dewetting, causing the transmission curve to more closely match the deposited layer, except for the longer wavelengths where transmission increased due to void formation. The thin film sample, where no annealing was conducted, shows a trend of Au absorption related to the imaginary component of the refractive index of Au. However, annealing at 400 °C and 500 °C, dewetting becomes more complete, forming larger Au nanoparticles or islands. These larger features create stronger plasmonic effects and alter the surface periodicity more significantly, resulting in a noticeable transmission dip (around 500–600 nm in this case) due to scattering. These larger features shift the interaction with light to longer wavelengths, which is evident from the redshift in the transmission curve. At the same time, larger features scatter light more, reducing transmission efficiency across some shorter wavelengths, which explains the flattening of the curve at lower wavelengths.

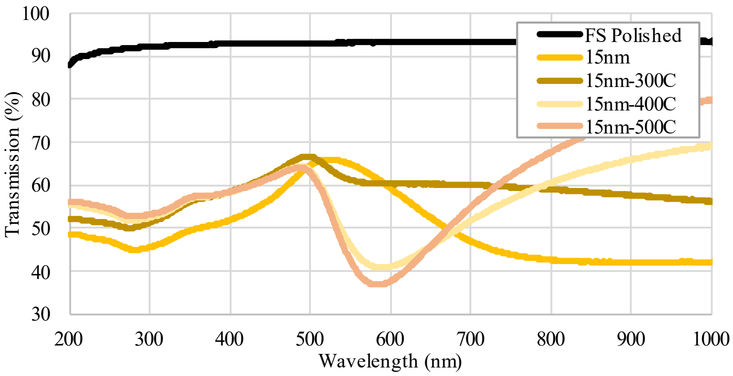

Figure 19: Measured transmission spectra for a blank unprocessed fused silica substrate, a substrate with 15nm of Au deposited, a substrate with 15nm of Au annealed at 300 °C, 400 °C and 500 °C. Each transmission curve has distinct trends after the Au absorption peak that are directly dependent on the size of Au islands formed. All measurements were taken at normal AOI with Agilent, CARY 60 spectrometer.

The transmission curve shifts to higher wavelengths as the Au feature size increases because of a few key factors that go along with increasing the scale of surface features in nano-structured coatings. The arrangement of submicron structures on the surface (the periodicity) causes interference between incoming light waves and the reflected waves. For certain wavelengths of light, these structures can suppress reflection by causing destructive interference. The effects of increasing Au feature size and periodicity is shown in Figure 20, where the transmission curve shifts to higher wavelengths.

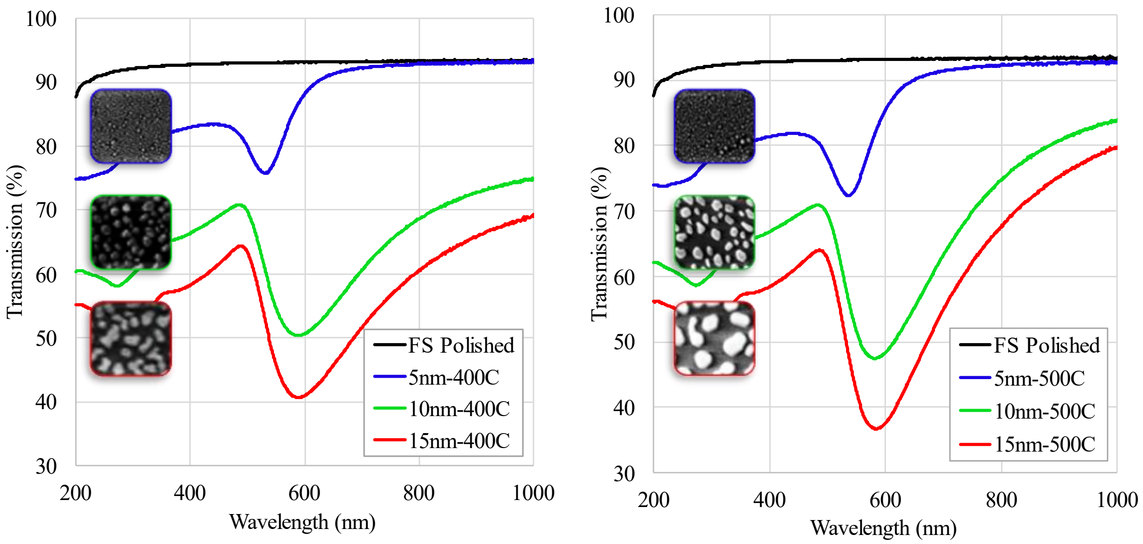

Figure 20: Resulting transmission spectra for metal masks consisting of three Au deposition thicknesses (5, 10, and 15nm) annealed at two key temperatures (400 and 500 °C). All measurements were taken at normal AOI with Agilent, CARY 60 spectrometer.

Another interesting trait of these metal masks is how the visual color of the sample changes due to interference effects (Fig. 21). When the gold is freshly deposited as a thin, continuous film (before annealing), the color you see is a result of thin-film interference and the color of gold itself. The incident light reflects off both the top surface of the gold layer and the interface between the gold and the fused silica substrate. The thickness of the gold layer determines which wavelengths of light interfere constructively or destructively, giving the film a distinct color. For very thin gold films below 15 nm, this interference often results in a blue or violet appearance because blue light is more strongly reflected while red light is more absorbed or interfered destructively.

When the thin film of gold is annealed, the continuous layer of gold undergoes dewetting, where the uniformity of the film is broken and the resulting nanoparticles support localized surface plasmon resonance (LSPR), where the resonance depends on the size, shape, and spacing of the gold nanoparticles, altering the visual color seen on the substrate (Fig. 21).

Figure 21: Fused silica substrates with various metal masks fabricated on the surface. The wide range of colors are a result of a wide range of Au feature geometries and spacings.

The metal masks generated with different feature sizes and structures all translate to different ARSS performance. The experimental results found during this study by fabrication of Au features on smaller optics can be transferred to large scale optics where invasive imaging/analysis of metasurface features are not readily available. Because of the randomness of the structure generation process, we can correlate the SEM images and transmission spectra produced from these small optic samples to verify masking on larger optics with consistency and confidence.

2.2.2 Precise Control of Metal Mask Features Through Repetitive Deposition and Annealing to Increase Mask Fill Factor

Another key concept that was explored within the scope of this masking research was the effects of repeated deposition and annealing. Again, the substrates chosen for this study were 1-inch-diameter, 0.0625-inch-thick double-sided polished Corning 7980 fused silica windows (Quartz Plus, Inc., Brookline, NH, USA). The three initial deposition thicknesses of 5, 10, and 15 nm were annealed, and imaged via SEM. The same Au initial thickness was then deposited over the once annealed islands and annealed again. This process was repeated for up to 4 times, referred to as “rounds”. These rounds represent iterative steps of deposition and annealing at the same thickness and temperature. While various annealing temperatures were studied, Figure 22 shows SEM images collected for a single maximum temperature for direct comparison. Table 2 contains the analytical results from analyzing the SEM images. The mean of all round periodicities for the same initial deposition thickness is shown in the left column of Table 2.

The results show that each iterative step of deposition and annealing correlates with an increasing fill factor for the mask features on the substrate, while still maintaining the periodicity established by the seed or first dewetting process. This is a very important result because of the dependency on the unit structure within the final ARSS transmission. Higher fill factor within these periodicities allows for a deeper etch depth that will alter the scattering effects for the ARSS performance as well.

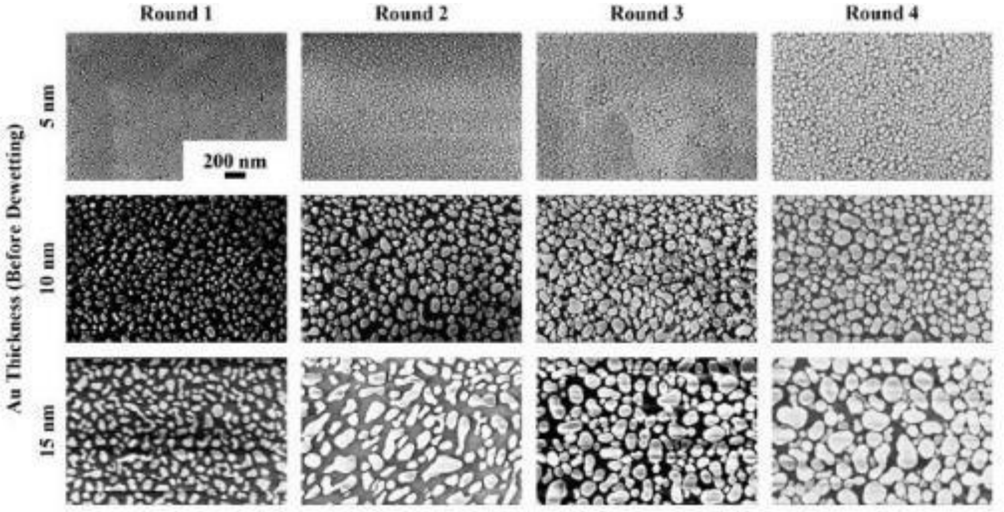

Figure 22: SEM images of multiple rounds of Au mask fabrication on FS substrate for initial and subsequent deposition thicknesses of 5, 10, and 15nm. The columns represent the iterative steps or rounds 1-4 of deposition and annealing at 400 °C. The rows represent the amount of Au deposited for each round. The images are of the same scale and were taken at 50,000x magnification in the center of the substrate. Some imaging artifacts can be seen, due to charging of the non-continuous conductive surface.

It is worth noting that the only results that did not follow the trend of stable periodicity were the 15 nm deposition rounds. Annealing temperature is a determining factor in the efficiency of the island formation, where higher deposition thicknesses required higher temperatures to generate circular Au islands. However, even at the lower annealing temperature the increasing fill factor trend still held true. Analysis of the surface features present during each step of this iterative process shows a trend of increasing fill factor and average diameter, while roughly maintaining the island spacing or periodicity.

Table 2: Island mask parameters obtained via image analysis

	Round	Avg. Equivalent Dia. (nm)	Periodicity (nm)	Fill Factor
Dep. Thickness Per Round: **5 nm** Periodicity: **34 ± 9 nm**	1	12	23	10%
	2	18	35	24%
	3	26	44	33%
	4	34	34	50%
Dep. Thickness Per Round: **10 nm** Periodicity: **91 ± 6 nm**	1	44	94	18%
	2	62	96	39%
	3	61	90	47%
	4	79	84	49%
Dep. Thickness Per Round: **15 nm** Periodicity: **131 ± 39 nm**	1	72	80	18%
	2	120	165	37%
	3	116	122	47%
	4	111	159	48%

For ARSS, the short end scattering edge wavelength is related to the feature sizes, while the transmission enhancement is related to the depth of the etch or features. Taller features extend the gradient-like refractive-index effect, suppressing reflection and altering the scattering effects at shorter wavelengths (Chapter 3). As shown in Figure 23, where the measured transmission spectra for masks of the same periodicity but increasing island size and fill factor correlates to shifts in the scattering edge of the spectral transmission curve to higher wavelengths. The transmission curves for the 10 nm metal mask annealed at 400 °C and 500 °C are similar due to the Au islands having comparable size and scale, as seen in Fig. 18.

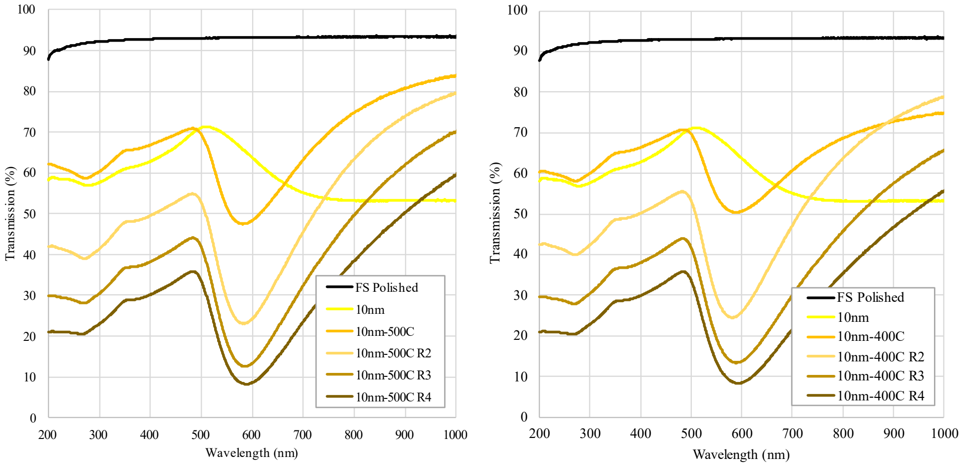

Figure 23: Measured transmission spectra for a blank polished fused silica substrate, a substrate with 10 nm Au without annealing, and four repetitive rounds of deposition and annealing at 10 nm and 400/500 °C, respectively. The transmission curves for each case are all similar due to the Au islands having comparable size and scale, as seen in Fig. 19. All measurements were taken at normal AOI with Agilent, CARY 60 spectrometer.

Tunability of specific wavelength transmission capabilities on the scale of tens to hundreds of nanometers is achievable through this method of metal mask fabrication. Etching these masked samples resulted in broadband transmission enhancement that can be applied to many different extremely specified applications.

While only a limited case is presented, there is an array of dewetted mask and etching parameters. Varying deposition thicknesses and annealing temperature between rounds would allow for a vast array of masking possibilities. There are instances where comparable masks could be formed with different methods requiring less rounds and overall fabrication time. Adjustable chemistry and etching chamber parameters also provide opportunities to realize high performance ARSS from these masks. More exploration and optimization is needed. Again, a major benefit of this controlled masking method is the scalability to large diameter and thick optics, often not practical with photo-lithography methods.

2.3 Summary of Metal Mask Control and Tunability

Experimental results from the fabrication of Au features on smaller optics can be transferred to large scale optics where invasive imaging/analysis of metasurface features are not readily available. From these Au masking results, we can correlate the SEM images and transmission spectra produced from these small optic samples to verify masking on larger optics with consistency and confidence. For an initial deposition thickness of 10 nm and repeated iterative steps of deposition and annealing, the fill factor increased (28%, 39%, 47%, 49%), while the island periodicity was maintained at average 91 ± 6 nm for all iterative steps. A comprehensive database of masking layer fabrication, resultant surface feature dimensions, and ARSS transmission enhancement capabilities was generated. This scalable masking approach enables tunable anti-reflective structured surfaces (ARSS) for high laser damage threshold applications, limited only by the size of deposition systems and annealing ovens.

CHAPTER 3: DETERMINATION OF RIE PLASMA ETCHING PARAMETERS FOR EFFICIENT ARSS FEATURE FORMATION

Production of these metasurface structures requires a material removal process where a metal mask is deposited, then etched away to generate a monolithic structure (Fig. 24). The portion of the silica substrate where no gold (Au) mask is present will be etched directly while also slowly etching the Au islands or cap layer, resulting in a cone-like array of structures directly mirroring the mask layer. However, if the etching is exceedingly deep and too much material is removed from the substrate, after gold mask layer depletion, causing the pillars to be destroyed or altered, the reflections become more prominent and result in transmission decrease. Therefore, the optimal ARSS performance should be observed shortly after mask depletion. This was tested by incrementally etching the metal masked fused silica substrates while monitoring the formation of ARSS.

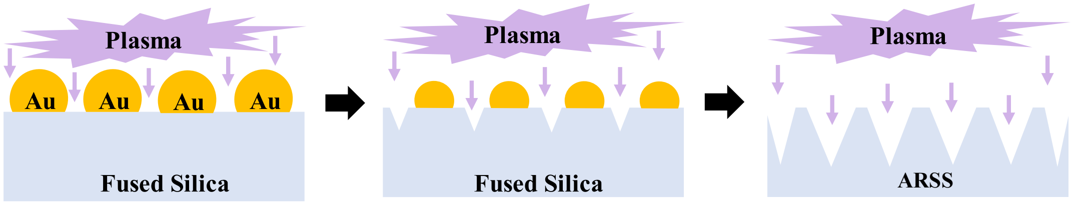

Figure 24: Processing steps for ARSS formation via metal masking and direct plasma etching. The portion of the mask not covered with Au islands will etch faster, resulting in pillar-like structures formed on the substrate once the mask is fully depleted.

In this approach, a PlasmaTherm RIE 7000 system is used to etch the masked silica. Since fused silica reacts well with fluorine- or chlorine-based gases, various gas compositions were tested for effective etching. Optimal ARSS performance occurs just after mask depletion, therefore, incremental etching for each mask recipe was applied to determine the ideal conditions for ARSS formation.

The etching process consists of five key steps. First, the chamber is evacuated to the target vacuum level in the depressurization phase. Next, during stabilization, the process gases are introduced, and their concentrations are confirmed. Plasma is then ignited by applying power. The substrate undergoes plasma etching for the specified duration, followed by a termination phase where the power is ramped down, and the chamber is purged. This sequence ensures precise control over the etching environment and process parameters.

3.1 Plasma Gas Chemistry

While plasma etching of fused silica using an Au mask, the choice of gas combinations plays a crucial role in determining the etch rate, surface morphology, and overall process efficiency. Substrates consisting of silicon react best with fluorine- or chlorine-based gases, therefore, this section explores the effects of three distinct gas mixtures (SF_6 and O_2, CHF_3 and O_2, and Ar and O_2) on the etching characteristics of fused silica. Chlorine was not readily available for this study; therefore, the scope of this work is focused on fluorine-based etching. Each gas combination brings unique chemical interactions and physical properties to the etching process, influencing the etch profile and selectivity. Oxygen was added to each of the recipes to enhance the removal of organic materials and promote the formation of volatile etch byproducts and keep the chamber walls oxidized. By comparing the etching speeds of each of these gas combinations, we aim to identify the optimal conditions for achieving precise and efficient etching of fused silica, contributing to the greatest control of ARSS feature formation.

For control, the etching parameters for all three gas combinations were consistent for each of the etching steps. The pressure and RF power levels used were 25 mT and 500 W, respectively. Etching was completed in steps of 5 minutes with the resulting transmission spectra measured between each step (CARY 60, Agilent). The substrate used was 7980 1”x1/16” Fused Silica and all were processed with the same metal mask at the same time. The mask recipe used for all gas combinations was a gold deposition of 10nm, annealed at 500 °C (see Chapter 2 for mask details).

Plasma etching of fused silica with an Ar plasma tends to be faster compared to using SF6 due to the distinct physical and chemical interactions involved. Argon ions contribute primarily through physical sputtering, where energetic Ar ions bombard the silica surface, breaking the Si-O bonds and physically removing material. In contrast, $\mathrm{SF_6}$ and $\mathrm{CHF_3}$ are fluorine-based plasma that rely more on chemical etching mechanisms. The gas dissociates into reactive fluorine radicals that chemically react with silica to form volatile silicon fluoride ($\mathrm{SiF_4}$) compounds. Additionally, the chemical etching rate can be limited by the availability and diffusion of reactive fluorine species to the silica surface, making it less aggressive compared to the more direct physical sputtering in the Ar plasma.

This difference in etching rate can be seen through the transmission spectra resulting from each etching step (Fig. 25). After just 10 minutes of etching with Ar plasma, the Au mask is almost completely depleted, producing a transmission spectrum like that of the blank unprocessed fused silica substrate.

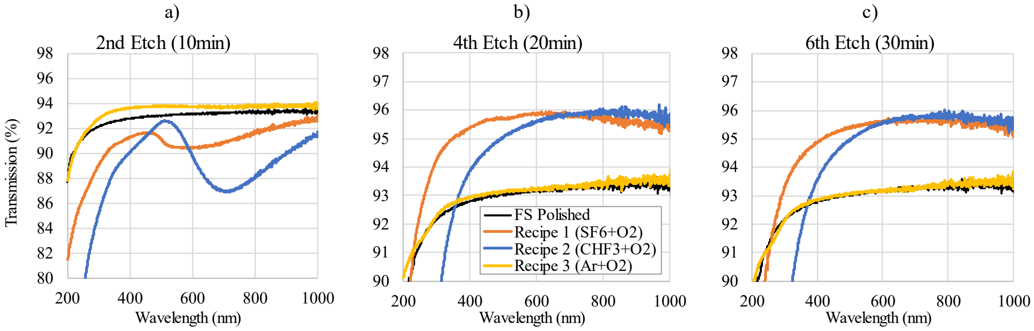

Figure 25: Transmission spectra comparison for 5-minute increments of etching for three different plasma etching gas combinations. The black, orange, blue, and yellow data represents an unprocessed fused silica substrate, substrate etched with SF_6 and O_2, substrate etched with CHF_3 and O_2, and substrate etched with Ar and O_2, respectively. All measurements were taken at normal AOI with Agilent, CARY 60 spectrometer.

If we take a closer look at the incremental etches completed for the first recipe (Fig. 26), we notice the transmission spectra shows an initial increase in transmission as the metal mask is gradually etched away in 5-minute steps, allowing the underlying ARSS to begin forming. In the early etching rounds, the spectra resemble that of the metal mask itself, characterized by lower transmission due to reflective metal. As etching progresses, transmission gradually increases, indicating the development of ARSS. However, after a certain depth is reached, prolonged etching begins to degrade the ARSS pillars and expose more of the substrate, leading to a decrease in transmission. This reduction suggests that the ARSS structures are over-etched, flattening the ARSS features, compromising the anti-reflective effect. The optimal ARSS performance thus occurs either just before or shortly after initial mask depletion.

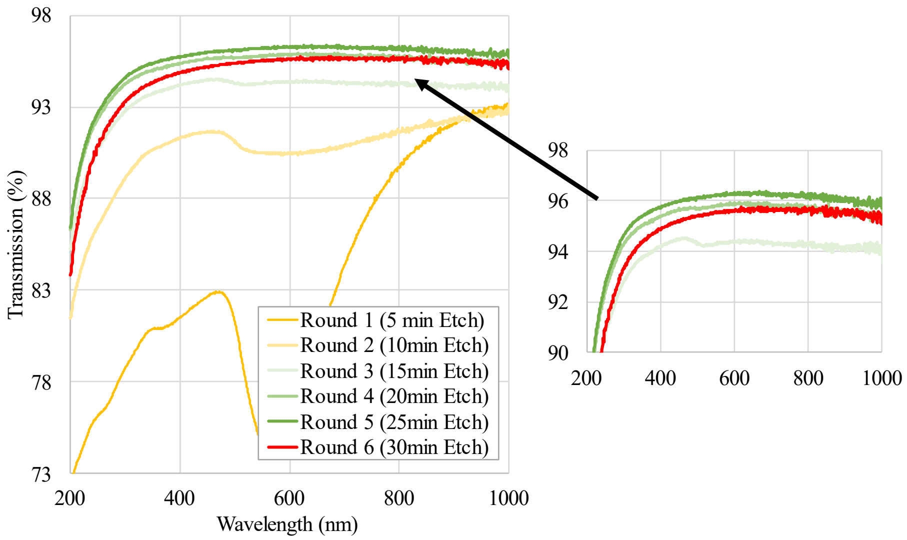

Figure 26: Measured transmission spectra resulting from plasma etching with the first recipe (SF_6 and O_2) in 5-minute increments on metal masked fused silica substrate. The formation of ARSS features can be tracked by the increase in transmission and sudden drop after excessive etching. All measurements were taken at normal AOI with Agilent, CARY 60 spectrometer.

The SEM images (Fig. 27) illustrate the progressive formation of ARSS during the etching process. In the initial stages, the structure closely resembles the original metal mask, with scattered, rounded islands lacking sharp definition. As etching advances, the mask begins to thin, and features on the silica surface become more pronounced. By the final etch rounds, distinct, sharp-edged pillars have formed, creating a well-defined ARSS pattern. These later etches show highly structured and separated features, indicating the mask's complete depletion and the formation of high-aspect-ratio structures on the substrate, characteristic of ARSS, which enhances the anti-reflective properties.

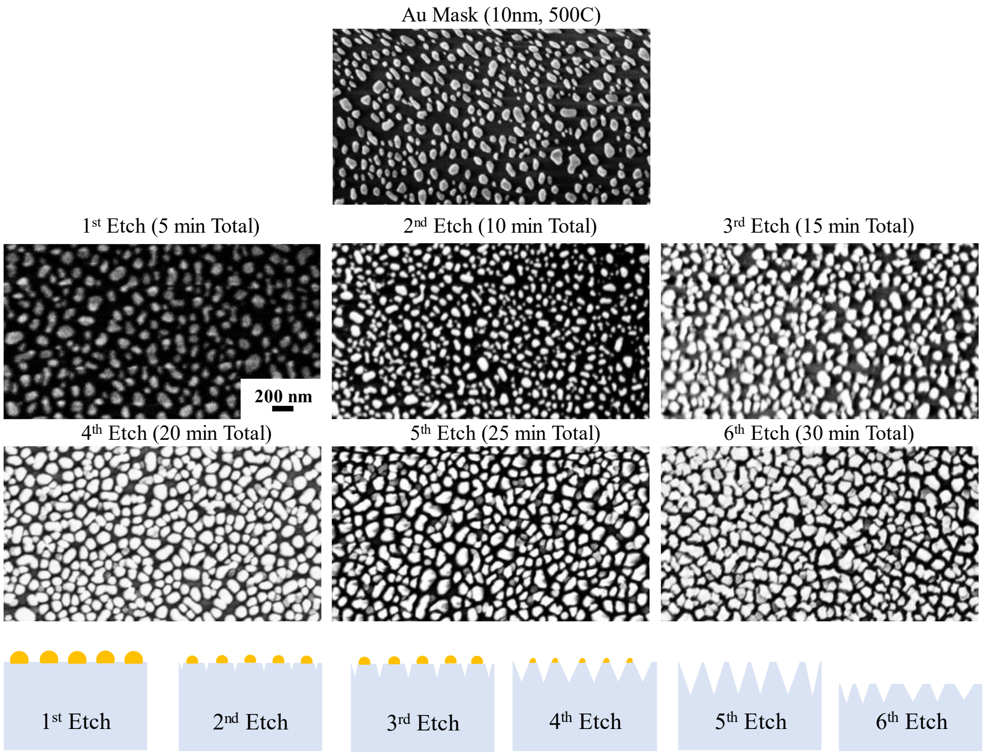

Figure 27: Scanning electron micrographs taken at each 5-minute etching step for the first etching gas recipe (SF_6+O_2). Au islands are being etched away, leaving behind ARSS structures on the fused silica substrate until a point is reached where continual etching will etch away the features, decreasing transmission. Images were taken at 50,000x magnification.

By directly comparing the transmission spectra and SEM images taken for each of the etching steps, we can track the formation of the ARSS features and see when the peak performance is achieved. The third recipe consistently shows the fastest etch rate of the Au mask, supporting the idea that $\mathrm{Ar} + \mathrm{O}_2$ plasma leads to more aggressive etching, likely due to the physical sputtering by Ar ions. The fluorine recipes show lower responses compared to argon because these recipes are chemically driven, resulting in slower rates compared to the physical sputtering mechanism.

Etching gas recipe of SF_6 and O_2 was chosen for continuing the research because of best controllability of etch speed. Having better control of the etching speed of the substrate allows for further tunability of the ARSS height. Now that a plasma etching recipe has been established, further exploration into the etching times needed for each of the metal masks generated in previous studies was needed.

3.2 Selective Transmission Enhancement: Nano-scale Unit Structure Dependence

3.2.1 Plasma Etching Until Metal Mask Depletion

As discussed in Chapter 2, island size and spacing are shown to increase with increasing initial Au deposition thickness, therefore, understanding the etching requirements for each mask of varying thickness was needed to further understand the evolution of how these ARSS features take shape. Three Au metal masks of thickness 5, 10, and 15nm all annealed at 500 °C were the focus for this portion of the study.

Etching these three metal masks was completed in steps of 5 minutes with resulting transmission spectra measured between each step (Agilent, CARY 60). This provides an idea of the required etching time needed based on the amount of Au deposited on the substrate. As was seen from the etching recipe study, the transmission was shown to gradually increase as silica moth-eye structures formed with each etch step. Also, we know that the Au masking layer has not been fully depleted because the absorption peaks (~500-600 nm) are still present. Once this absorption peak is minimized, the moth-eye pillar structures are taking shape as the etch gets deeper. The transmission spectra resulting from the etch steps compared to that of the blank silica show a steady increase in the transmission after each 5-minute etching step is seen until all the Au was gone. This leads to the conclusion that the ideal etching time for each masking and plasma combination is around 20-25 minutes for 5 and 10 nm, and around 40-45 minutes for 15 nm. An additional 5 minutes of etching resulted in ~1% decrease for the wavelength band tested.

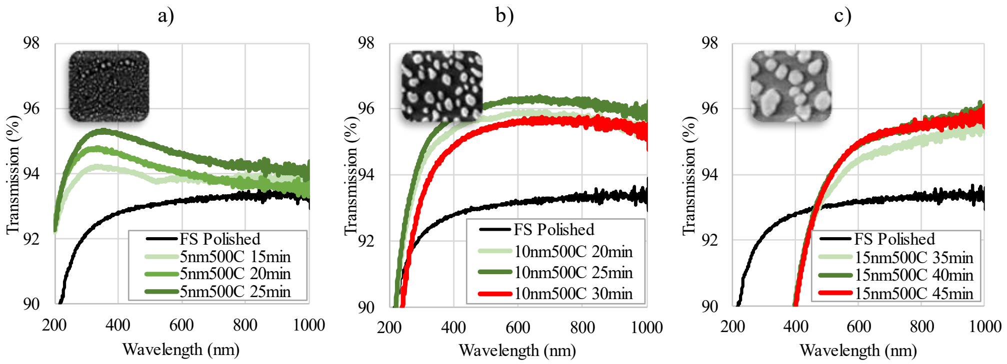

Figure 28: Measured spectral transmission for etching in 5-minute increments for a) 5nm Au thickness, b) 10nm Au thickness, and c) 15nm Au thickness, all annealed at 500 °C. The SEM images at the top of each are the metal masks being etched. All measurements were taken at normal AOI with Agilent, CARY 60 spectrometer.

Looking at the 10 nm mask, at ~600 nm wavelength, the 20 minute and 25 minute etches showed a 2.89% and 3.31% increase in transmission capabilities with respect to the blank sample, respectively (theoretical maximum being 3.65%). However, etching for an additional 5 minutes (30 minutes total) resulted in only a 2.59% increase with respect to the blank sample (0.70% decrease from previous etching step). This decrease is due to the destruction of the ARSS features. ARSS features that are generated on the surface of silica substrate will increase the overall transmission capabilities when compared to a standard blank sample. Also, there exists a shift within the peak transmission wavelength with respect to specific masking parameters that will be explained in the next section.

Understanding the etching requirements for each of the masks with variable Au thickness helps for controlling the ARSS formation and in turn the performance. Knowledge of how long to etch for each mask is necessary in generating a repeatable step by step process for ARSS fabrication. Correlating ARSS fabrication steps with performance will allow efficient manufacturability for transferring these steps to other substrates. Next, a further look into the specific waveband performance of etching these Au masks was completed.

3.2.2 Control of Peak Transmitting Wavelength

Once determination of the plasma etching parameters needed for each of the Au masks was completed, analysis of the optical transmission was tested. Each of the Au masked substrates were etched in the plasma chamber for various durations, coinciding with the results from the previous studies. Analysis of these SEM images was completed via the same methods discussed within Chapter 2. However, the height of these ARSS features was measured with an Olympus LEXT microscope. This tool has a limited lateral resolution, therefore, some of the samples with smaller features (specifically the ones generated from etching 5 nm Au thickness masks because they are on the same scale of and optimized to transmit the UV light used during the scan) were not able to be measured sufficiently. These feature heights were estimated by measuring the images taken at 45° (Fig. 29).

By comparing the SEM images of the Au mask and the final ARSS formed after etching (Fig. 29) we see that the ARSS lateral feature dimensions for the 10 and 15 nm initial deposition thicknesses appear to match well compared to their masks. However, the 5 nm initial deposition and dewetted islands were much smaller compared to the ARSS features transferred to the FS after etching. Our speculation is the inherent heat in the plasma etching process further annealed the mask while etching. For all the etches performed with this glass, there appeared to be a minimum ARSS pillar or feature width, regardless of whether the island mask used had smaller dimensions. Any ARSS with features smaller than shown in Figure 27 (bottom left) were not pillars, but instead holes. ARSS shown was etched with same etch chemistry and until Au mask depletion.

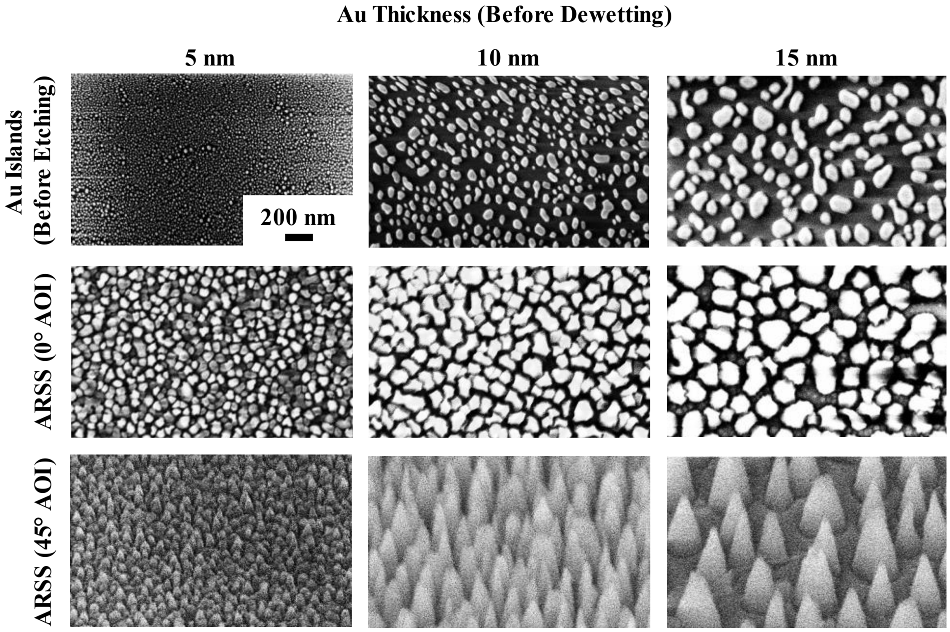

Figure 29: SEM images of each Au metal mask and corresponding ARSS after etching. The top and middle rows are taken at 0° AOI, the bottom row at 45° AOI. All images were taken at 50,000x magnification.

When comparing the SEM image analysis data (Table 3), we see the same trend of increasing feature size and spacing as the gold deposition thickness increases with the results of the Au masking study. For the 5 nm Au thickness, the resulting ARSS structure has an average equivalent diameter of 44 nm and periodicity of 75 nm, with minimal height development that was unresolvable for our microscope used. As the Au thickness is increased to 10 nm, the average diameter and periodicity grow to 75 nm and 106 nm, respectively, with a significant increase in feature height to 326 nm. For the thickest Au layer (15 nm), the average diameter and spacing further increase to 106 nm and 156 nm, with the tallest structures reaching 518 nm. This progression suggests that thicker Au deposition promotes the formation of larger, more widely spaced features in the ARSS pattern, likely due to the increased mass of the metal islands that spread further during dewetting and etching.

Table 3: ARSS feature parameters obtained via image analysis

ARSS Recipe	Avg. Equiv. Dia. (nm)	Avg. Periodicity (nm)	Avg. Height (nm)
5nm Au-500C-25min	44	75	122
10nm Au-500C-25min	75	106	326
15nm Au-500C-45min	106	156	518

The optical transmission of these three ARSS samples were measured and shown compared to polished blank sample (Fig. 30). The blank FS sample has two main Fresnel reflection losses from the front and back surface; therefore, a theoretical maximum single-side AR enhancement was approximated as the square-root of the double-side polished blank sample, shown in gray.

The peak transmission enhancement was measured in the ultraviolet, visible, and infrared for the initial deposition thicknesses of 5, 10, and 15 nm, respectively. For the visible regime, the 10 nm mask thickness showed a broadband enhancement with a peak transmission around λ=650 nm, 97% of the theoretical maximum (Fig. 30). The larger the ARSS features, the more scattering occurs and dominates the loss in transmission at shorter wavelengths. However, larger mask features allow for deeper etching and taller ARSS pillars to increase transmission at longer wavelengths. This trend established by the theoretical models previously discussed in Chapter 2, holds true for the experimental data presented.

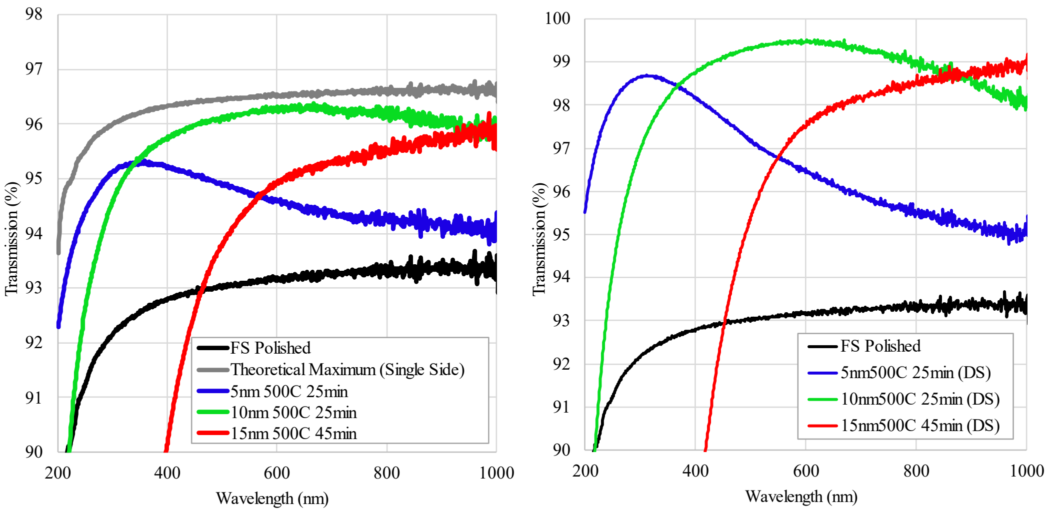
a)

b)

Figure 30: Measured spectral transmission for ARSS processed on fused silica for a) single-side (SS) and b) double-side (DS) fabrication. All measurements were taken at normal AOI with Agilent, CARY 60 spectrometer.

Fabricating ARSS on both sides of the FS substrate significantly increases the transmission while still maintaining the wavelength peaks that are produced through the periodicity established by the masking step. Again, the peak transmission enhancement was measured in the ultraviolet, visible, and infrared for the initial deposition thicknesses of 5, 10, and 15 nm, respectively. Each has significant enhancement and achieving close to if not above 99% total transmission (Fig. 30).

Further control of this peak transmitting wavelength can also be achieved by multiple steps of masking which, as explained in chapter 2, increase the size of the islands while still maintaining the periodicity established by the initial masking step.

3.2.3 Shift of Peak Transmitting Wavelength Through Repetitive Masking Steps

Further control of the ARSS performance based on etching the masks that underwent repetitive deposition and annealing was explored next. The idea is that the unit structure, or periodicity of the first masking step can be reinforced to allow for a deeper etch and therefore a taller ARSS feature. As the etch depth increases, the features become more effective at scattering light, particularly at shorter wavelengths. This scattering causes light to deviate from its original path, reducing the amount of light that is directly transmitted through the material. As a result, the transmission loss at shorter wavelengths becomes more significant. While deeper etching enhances scattering and potentially improves ARSS performance in reducing reflections, it also increases transmission losses at shorter wavelengths. This trade-off is crucial when designing ARSS for specific applications, as it may affect the balance between minimizing reflection and maintaining high transmission in certain wavelength ranges.

A comparison between the SEM images of the Au mask and corresponding ARSS formed gives a visual understanding of the effects of this repetitive masking (Fig. 31). Upon analysis of the ARSS features (Table 4), we demonstrate that repetitive masking increases the fill factor, or the amount of Au coverage, on the substrate while preserving the periodicity initially established in the first round of masking. For example, the average periodicity remains close to 110 ± 5 nm across all four rounds for the ARSS features. However, with each additional masking round, the average feature height increases significantly. Starting with an initial height of 326 nm in the first round (R1), the height increases to 399 nm in the second round (R2), 581 nm in the third round (R3), and slightly decreases to 523 nm in the fourth round (R4). This progressive increase in height supports that repetitive masking with a maintained periodicity allows for the development of high-aspect-ratio ARSS structures, enhancing the anti-reflective properties of the surface.

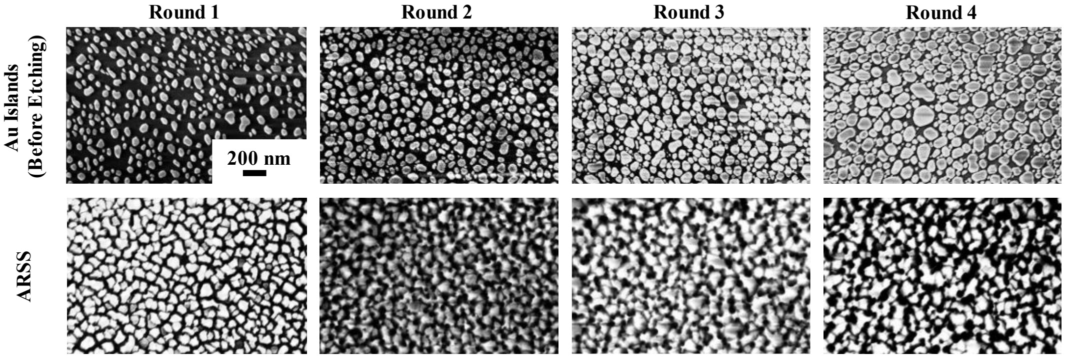

Figure 31: SEM images of repetitive Au masking for 4 rounds of 10 nm Au deposition followed by annealing at 500 °C (top row) as well as corresponding ARSS features left behind after etching for specified duration (bottom row). Images were taken at 50,000x magnification.

Table 4: ARSS feature parameters obtained via image analysis for repetitive masking

ARSS Recipe	Avg. Equiv. Dia. (nm)	Avg. Periodicity (nm)	Avg. Height (nm)
10nm Au-500C R1-25min	68	106	326
10nm Au-500C R2-45min	60	106	399
10nm Au-500C R3-55min	66	117	581
10nm Au-500C R4-65min	57	109	523

For the transmission spectra of each repetitive masking scenario (Fig. 32), we can expect different behaviors based on the height and density of the ARSS features. However, since the periodicity remains relatively stable, the overall spectral shape will remain similar, but with shifting transmission peaks as the feature height increases. As the height of the ARSS structures increases with each successive masking and etching round, the scattering edge in the transmission spectra is expected to shift toward higher wavelengths. For shorter ARSS features, scattering typically begins at lower wavelengths due to the limited transition gradient, causing a steeper drop-off in transmission. As the ARSS height increases, the wavelength at which significant scattering occurs shifts higher, pushing the edge of high transmission further into the visible or near-infrared regions. This effect means that taller ARSS structures can extend anti-reflective performance to longer wavelengths before reflection losses become pronounced.

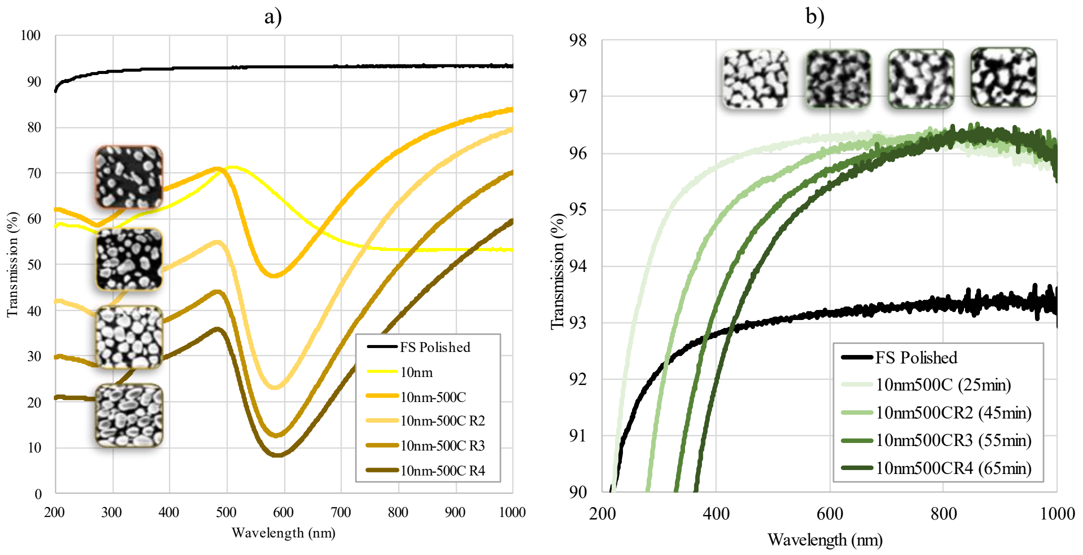

Figure 32: Measured spectral transmission for repetitive masking of 10nm Au annealed at 500 °C, a), as well as the corresponding ARSS after fully etching the Au mask, b). All measurements were taken at normal AOI with Agilent, CARY 60 spectrometer.

3.3 Summary of RIE Plasma Etching for ARSS Fabrication

Chapter 3 explores the optimization of RIE plasma parameters for creating ARSS on fused silica using a gold mask. From the results of this study, we can better understand the evolution of ARSS on fused silica based on the Au masking layer depletion and resulting plasma etch parameters. Using various gas combinations, the study compares their etching rates and effects on surface morphology as well as investigating etching durations required to prevent over-etching, which could degrade ARSS effectiveness. It was clear to see that as the Au was removed through the plasma etching process, the resulting structures did perform as expected based on the moth-eye effect, increasing the overall transmission. However, there does exist a point where the substrate is etched too deep, and flattening of the structures hinders transmission enhancement.

The optical transmission measurements showed significant improvement over a blank fused silica sample. For the 10 nm mask, peak transmission enhancement was achieved around 650 nm, reaching 97% of the theoretical maximum in the visible range. Thicker ARSS structures, such as those formed by the 15 nm mask, increased scattering at shorter wavelengths but were beneficial for deeper etching, supporting transmission at longer wavelengths. Additionally, the peak transmission wavelength could be shifted by performing multiple masking steps, which enlarge the islands while retaining periodicity. Repetitive masking increased the etch depth and ARSS pillar height, but also led to more light scattering, especially at shorter wavelengths, which reduced direct transmission. This trade-off is crucial for ARSS design in applications where minimizing reflection without compromising transmission across specific wavelength ranges is essential.

CHAPTER 4: TRANSFERING rARSS PROCESS

A key motivation for developing and expanding on this ARSS fabrication method is its adaptability to various substrates with minimal process changes. This has been proven effective on multiple optical glass substrates commonly used as optical components. Also, alternative metals such as Ag and Pt were evaluated for masking, revealing unique dewetting behaviors that influence ARSS formation. Scalability testing identified many needed adjustments in equipment capacity and process parameters, to enable successful transfer to a larger substrate.

4.1 Fabrication of ARSS on Various Silica Substrates

A few optical windows were tested for exploring the transferability of the ARSS fabrication processes described within this work. JGS2 fused silica, Corning 7979 fused silica, Corning 7980 fused silica, and BK7 glass are all optical materials commonly used in applications requiring high transparency, thermal stability, and precision. JGS2 and 7979 fused silica are Chinese and Corning equivalents, respectively, both having high purity, suitable for UV to near-infrared applications, and feature low thermal expansion [29, 30]. The 7980 fused silica, also from Corning, is an ultra-high-purity grade specifically optimized for extreme ultraviolet (EUV), and deep-ultraviolet (DUV), making it ideal for advanced lithography. BK7, on the other hand, is a borosilicate crown glass and differs from fused silica by having a higher refractive index and slightly lower UV transparency. BK7's higher index makes it a common lens material for lower weight.

While it has good optical clarity and lower cost than fused silica, it is more sensitive to thermal expansion, making it less suitable for high-heat or UV-intensive applications [29, 30, 31]. Overall, while JGS2, 7979, and 7980 are more like each other in terms of UV transparency and thermal stability, BK7 offers a practical alternative with some limitations, particularly in demanding UV or high-temperature environments.

Using the results from exploring the ARSS fabrication process completed within this work, significant transmission enhancements across all silica substrates were achieved (Fig. 33). Each substrate received Au deposition, dewetting, and plasma etching for producing ARSS optimized for peak transmission in the NIR region (700-1000 nm), with all treated samples showing improved transmission for single side processing compared to a polished, untreated sample. The only change in the recipe was using etch recipe #2 (CHF_3 and O_2) for the BK7 substrate due to chemical selectivity.

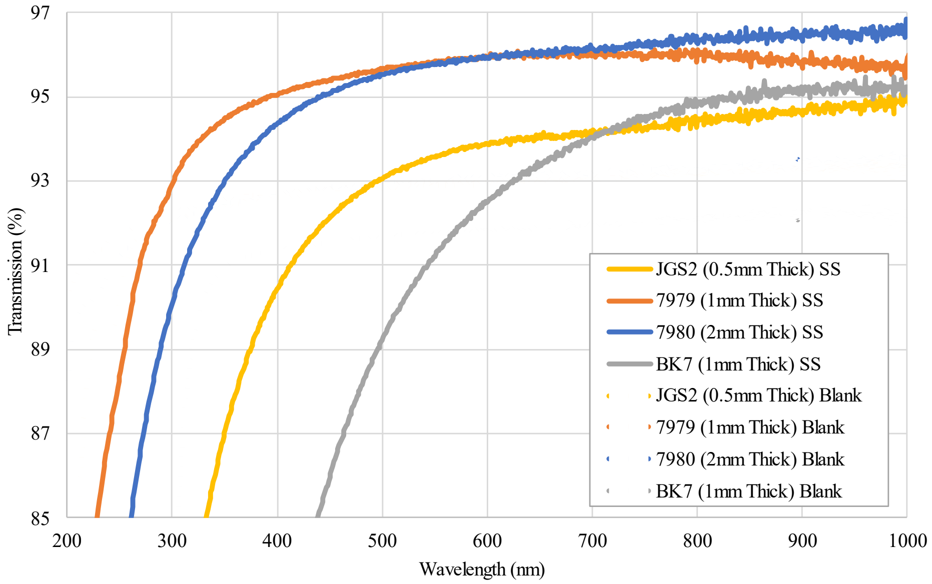

Figure 33: Measured spectral transmission for ARSS fabricated on four different silica substrates (JGS2, 7979, 7980, BK7). The ARSS recipe used was optimized for the NIR

region, with all treated samples show improved transmission within this range for single side processing.

These results enhance understanding of ARSS fabrication requirements across various optical window materials and expand the database for ARSS performance and manufacturing.

4.2 Exploration of Dewetting Other Metals

This research also explores using alternative metals to Au for metal masking. Dewetting studies were conducted on Ag, Pt, and Al films with thicknesses of 5, 10, and 15 nm to determine the temperatures required for dewetting and to compare their behavior with Au. Preliminary findings indicate differences in dewetting temperature and film morphology among the metals, which could offer insights into optimizing the ARSS fabrication process with alternative materials.

Gold has a melting temperature of 1,064 °C, therefore, dewetting can occur at relatively low temperatures, often around 300-400 °C. This lower dewetting temperature relative to its melting point is due to gold's strong surface diffusion properties, making it favorable for metal masking. Silver, with a melting temperature of 961 °C, also dewets effectively at lower temperatures, usually around 200-300 °C, which is again much lower than its melting point. Like gold, silver has high surface mobility, facilitating dewetting without requiring extreme temperatures. Platinum has a much higher melting point of 1,768 °C, and dewetting typically requires temperatures around 600-700 °C or higher.

This higher dewetting temperature reflects platinum’s lower surface diffusion compared to Au and Ag, which could impact processing conditions and stability. Aluminum (Al), melting at 660 °C, shows dewetting behavior at relatively low temperatures around 150-300 °C, close to those of silver. However, aluminum's tendency to oxidize quickly requires careful control of the environment during dewetting to avoid the formation of oxides that can inhibit dewetting.

These differences highlight how dewetting temperatures vary significantly by metal, with surface diffusion characteristics and oxidation tendencies playing key roles. Understanding these differences allows for much larger control of ARSS fabrication steps that translate to specific AR capabilities.

4.2.1 Dewetting of Platinum Thin Films

Due to the melting temperature of Pt being significantly higher than that of the other metals tested, the annealing temperatures that were chosen for the Pt dewetting were 800 and 900 °C. As was seen from the Au dewetting, the driving factors for island formation were deposition thicknesses and annealing temperature. As deposition thickness increases, the islands become larger and more irregular in shape, indicating a shift from finer, densely packed particles to coarser, more isolated structures. Like the Au dewetting results, this trend is due to the greater volume of Pt available for promoting the formation of larger islands. Additionally, higher annealing temperatures promote greater surface diffusion, leading to further growth and coarsening of the islands. In thinner films at lower temperatures, the islands remain smaller and more uniform. Together, deposition thickness and annealing temperature are critical factors driving the size, spacing, and morphology of dewetted islands, with higher values of each parameter favoring larger, more irregularly shaped islands (Fig. 34).

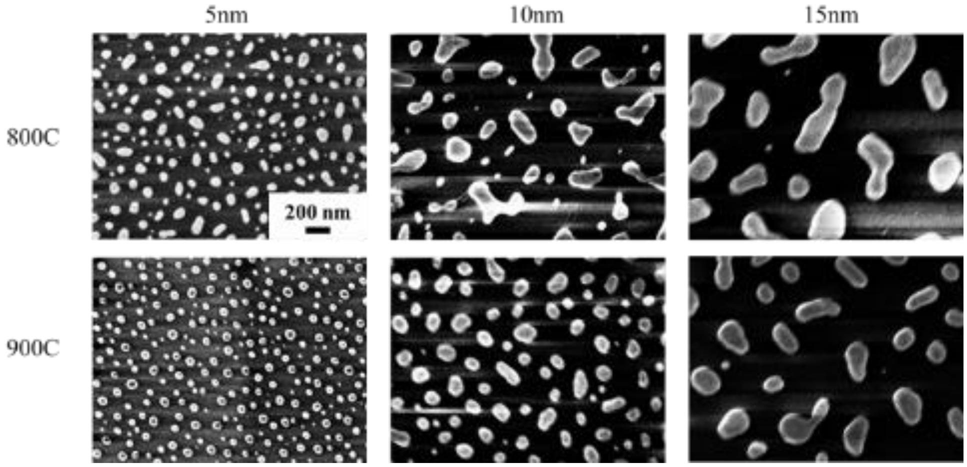

Figure 34: SEM images taken for each Pt deposition thickness (5, 10, and 15 nm) annealed at each temperature (800 and 900 °C). Images were taken at 50,000x magnification.

4.2.2 Dewetting of Silver Thin Films

The dewetting behavior of Ag again highlights the influence of deposition thickness and annealing temperature on island formation. As the thickness of the Ag film increases, the islands become larger and more widely spaced, indicating greater coalescence and material availability for forming individual islands. At higher annealing temperatures, the islands tend to become more rounded and less densely packed, as increased surface mobility allows the Ag particles to diffuse and coalesce more readily. In thinner films, island structures are smaller and more densely packed, as there is limited material to spread across the surface. These trends underscore that higher temperatures and greater thicknesses promote the formation of larger, well-separated islands, driven by enhanced surface diffusion and coalescence of Ag under thermal treatment.

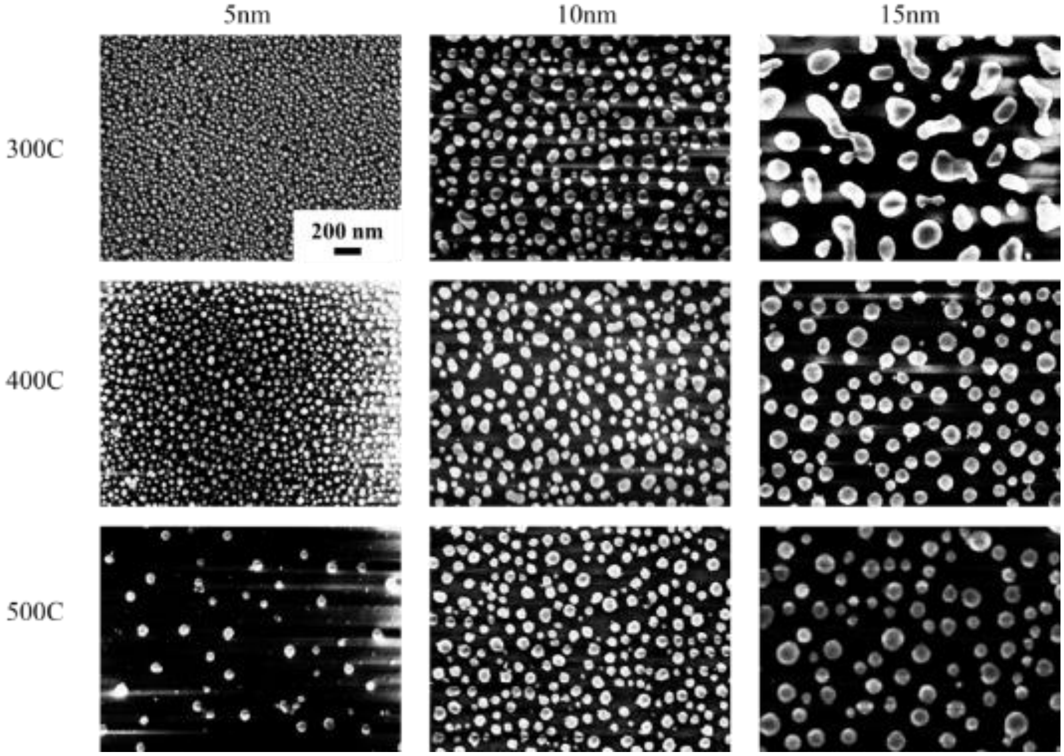

Figure 35: SEM images taken for each Ag deposition thickness (5, 10, and 15 nm) annealed at each temperature (300, 400 and 500 °C). Images were taken at 50,000x magnification.

Future work will explore etching requirements for other metals like Pt and Ag to understand how each metal mask influences ARSS formation during plasma etching. Literature shows Pt to have 5x the etch selectivity compared to Au, which can be beneficial for etching materials like sapphire.

4.3 Transferring ARSS Fabrication Process to Larger Optics

A key motivation for this fabrication process is its scalability to larger substrates. However, scaling requires adjustments to processing equipment, including specialized stages to hold large samples during deposition, annealing, and plasma etching (Fig. 36). These adjustments were completed to ensure uniformity and effectiveness on large-scale substrates.

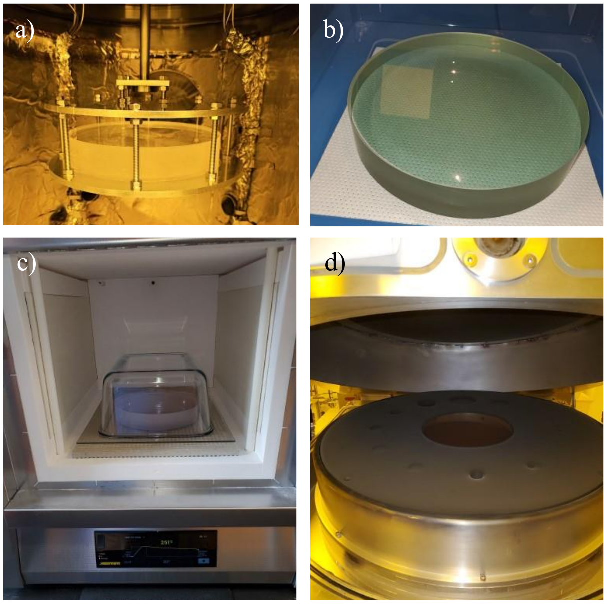

Figure 36: ARSS fabrication on large substrates. (a) Modified Lesker E-Beam stage for larger samples; (b) 8-inch diameter, 2-inch-thick optical window with Au deposition; (c) large furnace; and (d) custom graphite platen in PlasmaTherm 7000 for handling large substrates.

4.3.1 Adjustments to Metal Deposition Fixturing

For large substrates, the ARSS recipe required switching deposition equipment. While the AJA sputtering tool was initially used, its chamber size limits to optics under 6 inches. Thus, the Lesker E-Beam evaporator, which accommodates samples up to 12 inches in diameter, was employed. Modifications to the stage were necessary to support 8- to 12-inch diameter windows. A custom stage design (Fig. 37) was developed to securely hold these larger, thicker windows.

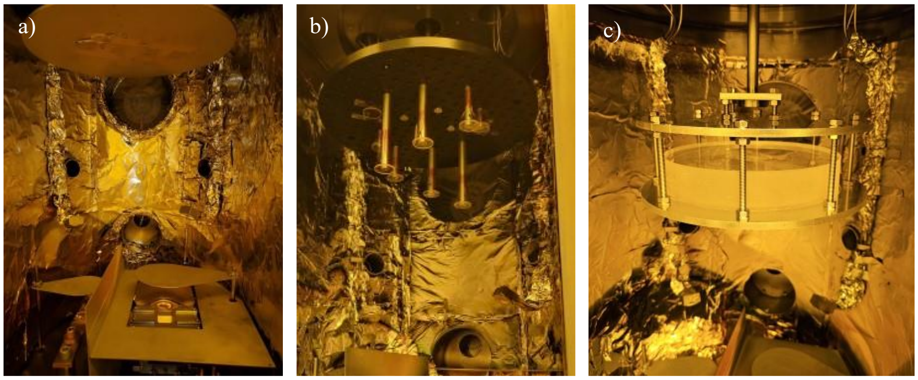

Figure 37: Comparison between Lesker E-Beam stage for a) small 1-inch diameter substrates and b) determination of scaling factor based on proximity to E-beam source, and c) large 8-inch diameter substates. A new stage was designed and implemented for scaling the metal deposition.

On large, thick substrates, proximity to the E-Beam source significantly affects deposition rate. When the substrate is positioned closer to the source (lowered stage), it receives a higher flux of material, causing a faster deposition rate than indicated by the equipment's thickness monitor, which is calibrated for substrates positioned farther away, such as at the top of the chamber. To address this, adjustments to deposition parameters were made to ensure accurate thin-film thickness on these large windows.

4.3.2 Adjustments to PlasmaTherm7000 for Etching

The PlasmaTherm 7000 etcher can hold large substrates, but the original graphite platen lacked the proper geometry for thick samples. Custom platens were designed and machined to support these larger samples (Fig. 38). The graphite platen plays a critical role in plasma etching processes, particularly for large-scale substrates. Its primary purpose is to evenly distribute temperature and provide stable support during etching, which is crucial for achieving uniform results across the substrate's surface. Graphite is chosen because of its excellent thermal conductivity, which helps prevent temperature fluctuations that could lead to uneven etching rates or structural distortions. Additionally, graphite is highly resistant to chemical reactions with the plasma gases used, ensuring that it remains stable and does not contaminate the substrate

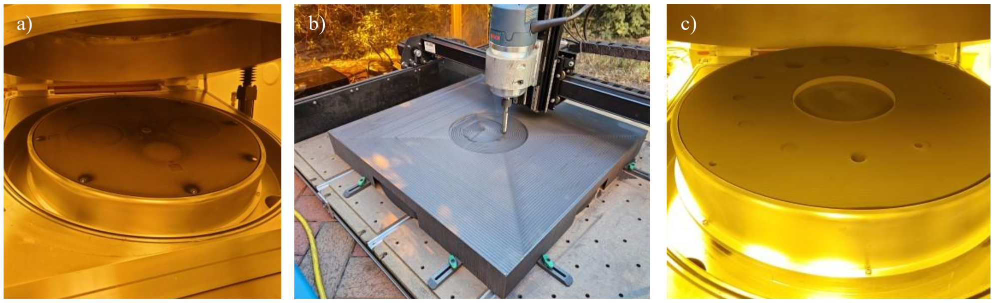

Figure 38: PlasmaTherm7000 graphite platen for a) small 1-inch diameter substrates, b) the machining of graphite for large substrates, and c) large 8-inch diameter substate within the PlasmaTherm7000. A new platen was designed and implemented for scaling the etching process.

For large, heavy windows, fabricating ARSS on both sides requires adjustments to the etching process. Direct contact with the graphite platen was avoided to prevent damage to features on the etched side, so a custom platen with a ring elevation was used to create this air pocket under the substrate. However, this air gap reduced the etch rate compared to smaller substrates, which sit directly on the platen. After several tests, it was found that etching until metal mask depletion was not feasible for large substrates. Instead, etching was done for a longer, fixed time, followed by an Au wet etch to reveal ARSS features.

4.3.3 Uniformity Test of ARSS on Large Windows

When transferring ARSS fabrication to large windows, limitations like uniformity in ARSS formation must be considered. Using a custom gantry system (Fig. 39), transmission at 532 and 1064 nm was measured across the surface of an unprocessed and an ARSS-single-side-processed 8-inch diameter JGS2 fused silica substrate (Fig. 40).

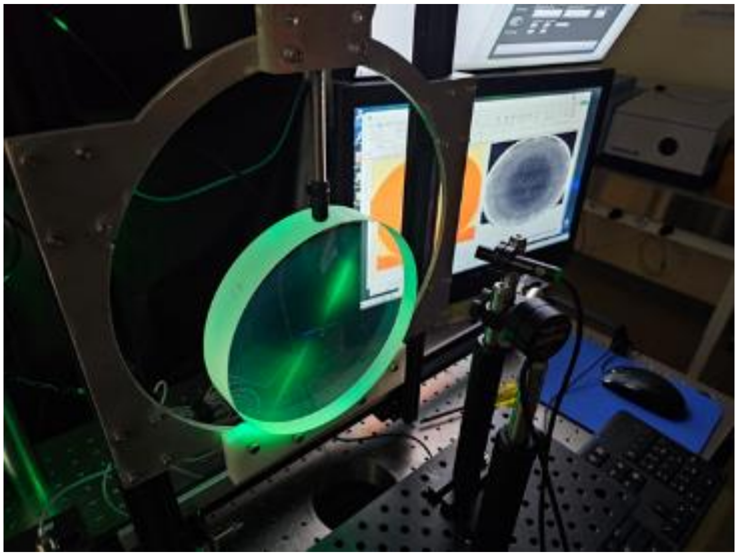

Figure 39: Custom gantry system used for ARSS uniformity analysis. The transmission was measured at 520 and 1064 nm, across the entire span of the optical window.

Although transmission enhancement was seen across the window, scanning results indicate a radial dependency in transmission on the ARSS-processed sample, likely due to nonuniform etching mentioned in previous section. The custom graphite platen for large window fabrication limits contact to the outer edge, creating a center pocket under the substrate, which slows etch rates and causes radial nonuniformity.

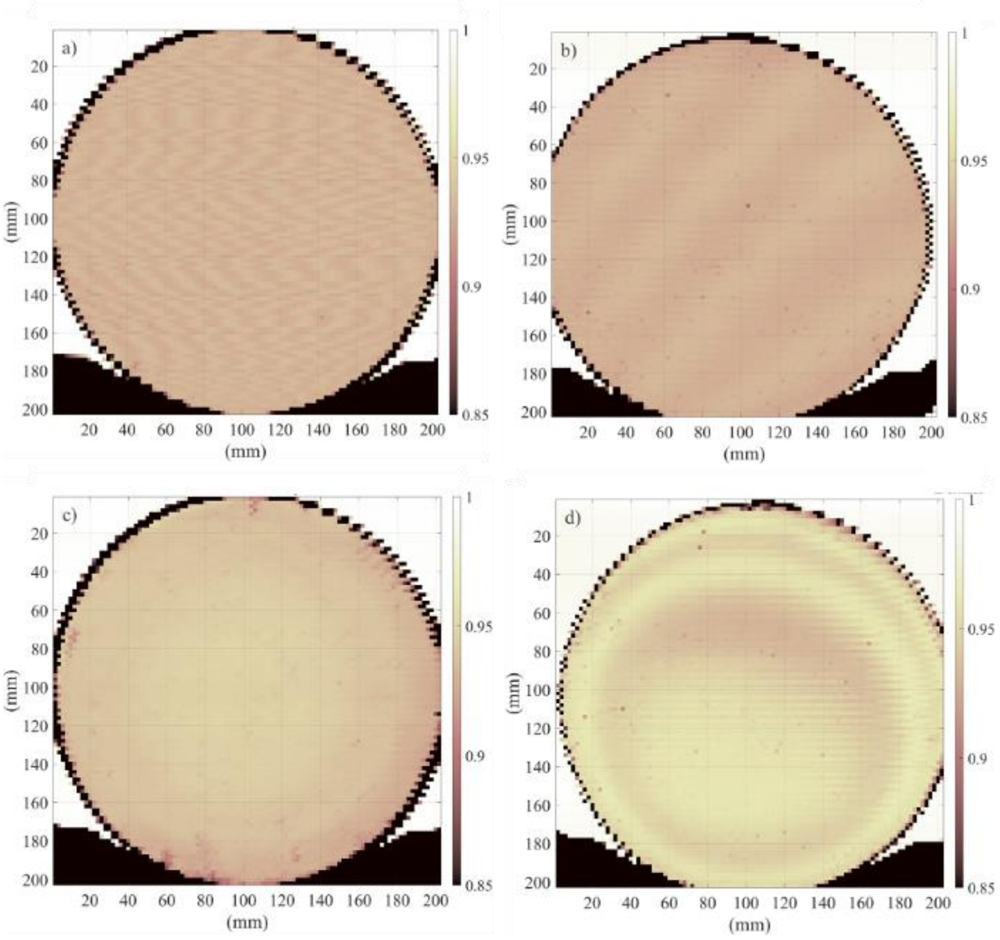

Figure 40: Measured transmission uniformity for 8in diameter by 1.5in thick JGS2 fused silica window, a) unprocessed measured with λ = 520 nm laser, b) unprocessed measured with λ = 1064 nm laser, c) ARSS single side processed measured with λ = 520 nm laser, and d) ARSS single side processed measured with λ = 1064 nm. The color scale bar on the

right indicates transmission values from 0 to 1. The ARSS recipe used was optimized for ~600 nm wavelength.

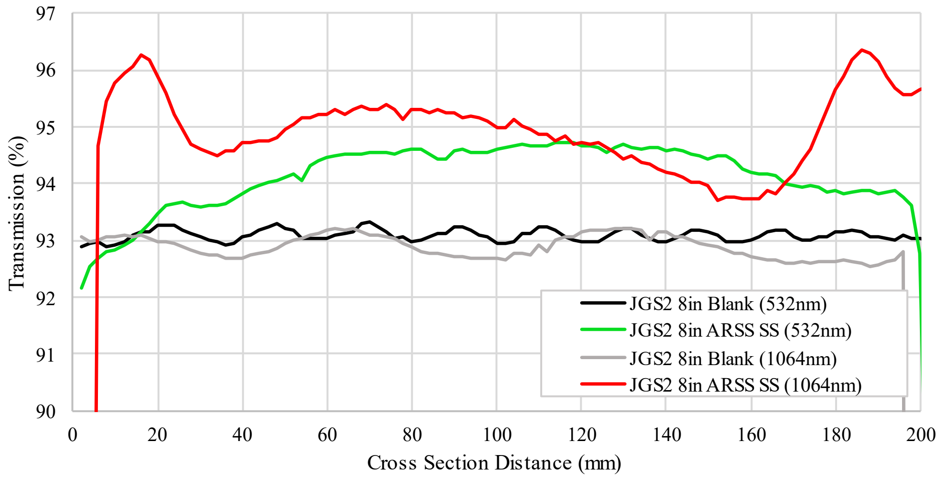

Figure 41: Measured cross section transmission for JGS2 8in diameter by 1.5in thick fused silica window, unprocessed (black/gray) and ARSS single side processed (green/red). The green and red data was measured with a 520 nm and 1064 nm laser, respectively. There is transmission enhancement seen, however, there exists a radial dependency on enhancement most likely caused by ununiform deposition or etching. The ARSS recipe used was optimized for ~600 nm wavelength.

The radial dependence in transmission for the ARSS-processed fused silica sample could be due to variations in the etching or deposition process across the surface. As the gantry moves in a scanning pattern, nonuniformities in processing parameters may create inconsistencies in the anti-reflective structure. This results in the transmission decreasing at the edges, likely due to less effective ARSS formation in those regions.

4.4 Summary of Transferring and Scaling ARSS Process

This chapter focuses on the transferability, scalability, and optimization of ARSS fabrication processes for large optical substrates as well as using various metals for masking. Various silica substrates, including JGS2, 7979, 7980 fused silica, and BK7 glass, were tested and significant improvements in transmission across these substrates were achieved after ARSS fabrication, demonstrating the effectiveness of the process for different materials. The results expanded the understanding of ARSS fabrication requirements and enhanced the database for ARSS performance.

The study also investigated the dewetting behavior of alternative metals, such as Ag, Pt, compared to Au, for metal masking. Differences in dewetting temperatures and film morphology were observed, with each metal exhibiting unique characteristics that could optimize ARSS fabrication. Future work will further explore the etching requirements for these metals, focusing on how each metal mask influences ARSS formation during plasma etching.

A key motivation for the research was the ability to scale the ARSS fabrication process to larger substrates. Several modifications to processing equipment, including the Lesker E-Beam evaporator and PlasmaTherm 7000 etching system, were made to accommodate substrates ranging from 8-inches to 12-inches in diameter. Custom stage designs and graphite platens were developed to ensure stability, uniformity, and effective processing. However, challenges like reduced etch rates due to air pockets under the substrate and the difficulty of etching until metal mask depletion on large samples were addressed by adjusting etching times and incorporating a wet etching step for excess metal mask removal.

This chapter concludes with a successful implementation of the ARSS process for large-scale substrates, providing valuable insights for scaling up the fabrication process. Uniformity testing was conducted on a large JGS2 fused silica substrate to evaluate the consistency of ARSS formation across the surface. This test showed one limitation being the radial dependency of the ARSS formation either due to inconsistencies in the masking or plasma etching step in fabrication. Future work will explore further optimizations, including mitigation of this radial dependency.

CHAPTER 5: CONCLUSIONS

This thesis explored the tunability of anti-reflective structured surfaces (ARSS) through advanced fabrication techniques, focusing on the integration of moth-eye structures, particularly in fused silica substrates. The collaborative research efforts at UNC Charlotte under the guidance of Dr. Aggarwal, Dr. Poutous, and Dr. Hutchens have led to significant advancements in ARSS technology, demonstrating both high durability and exceptional performance in laser applications. Initial investigations into the fabrication of random ARSS (rARSS) using gold masking techniques revealed promising results, with structures capable of withstanding laser power densities up to 70.7 MW/cm^2. LIDT observed for these ARSS structures was notably up to ten times higher than that of conventional thin-film anti-reflective coatings, nearing the LIDT of the bulk material itself. This finding underscores the potential of ARSS for high-performance applications in applications subject to intense laser exposure.

Key to the success of these applications is the ability to fine-tune the transmission capabilities of the ARSS fabricated on the surface of optical components. This work confirmed that altering fabrication parameters, such as deposition thickness and annealing temperature of the gold mask, allows for the control of peak transmission wavelengths while maintaining broad-spectrum enhancements. The creation of a comprehensive database detailing the relationship between masking layer characteristics and ARSS performance enables future research and production scalability. This foundational work supports the transition from small optics to larger systems, where in situ imaging and analysis of metasurfaces can pose challenges.

Optimization of RIE parameters highlighted the critical role of gas chemistry and etching duration in preserving the structural integrity of ARSS. Exploration of various gas chemistries, such as $\mathrm{SF_6}$ and $\mathrm{O_2}$, $\mathrm{CHF_3}$ and $\mathrm{O_2}$, and Ar and $\mathrm{O_2}$, provided insights into their differing etching rates and surface morphologies, illustrating the complex interplay between etching depth and ARSS formation. However, the findings also indicated the delicate balance required in ARSS design where excessive etching can compromise the structures, leading to reduced transmission.

Successful characterization of ARSS features on fused silica through metal masking and controlled plasma etching demonstrated substantial improvements in optical transmission, particularly achieving selective peak transmissions at or above 99% at various wavelengths based on the ARSS periodicity established in the masking step. Also, the study of iterative masking steps revealed a method for further control of island size while maintaining periodicity, allowing for effective manipulation of transmission characteristics across desired wavelength ranges.

In conclusion, this research demonstrates that ARSS fabrication and optimization through tunable parameters is not only feasible but also essential for advancing anti-reflective technologies across various commercial applications. The work establishes a robust framework for future investigations into ARSS, paving the way for innovations that harness their unique properties for high-performance optics and laser applications. The consistent results and comprehensive datasets generated herein will serve as valuable references for both academic research and industrial manufacturing, ensuring that the advancements in ARSS technology continue to progress.

REFERENCES

1. Perram, Glen P., Michael A. Marciniak, and Matthew Goda. *SPIE Proceedings*, September 10, 2004
2. Azadgoli, Beina, and Regina Y Baker. “Laser Applications in Surgery.” Annals of translational medicine, December 2016.
3. Cheng, Jian, Jinghe Wang, Jing Hou, Hongxiang Wang, and Lei Zhang. “Effect of Polishing-Induced Subsurface Impurity Defects on Laser Damage Resistance of Fused Silica Optics and Their Removal with HF Acid Etching.” *Applied Sciences* 7, no. 8 (August 15, 2017): 838.
4. Ghosh, Gorachand. “Dispersion-Equation Coefficients for the Refractive Index and Birefringence of Calcite and Quartz Crystals.” *Optics Communications* 163, no. 1–3 (May 1999): 95–102.
5. T. Aytug, A. R. Lupini, G. E. Jellison, P. C. Joshi, I. H. Ivanov, T. Liu, et al., "Monolithic gradedrefractive-index glass-based antireflective coatings: broadband/omnidirectional light harvesting and self-cleaning characteristics," J. Mater. Chem C, vol. 3, pp. 5440-5449, 2015.
6. S. Chattopadhyay, Y. F. Huang, Y. J. Jen, A. Ganguly, K. H. Chen, and L. C. Chen, "Antireflecting and photonic nanostructures," Materials Science and Engineering: R: Reports, vol. 69, pp. 1-35, 2010/06/20/ 2010.
7. Carr, C. W. et. al., “Localized dynamics during laser-induced damage in optical materials,” Physical Review Letters, 92(8), (2004).
8. Schubert, M. F., Poxson, D. J., Mont, F. W., Kim, J. K., & Schubert, E. F., “Performance of antireflection coatings consisting of multiple discrete layers and comparison with continuously graded antireflection coatings,” Applied Physics Express, 3(8), 082502 (2010).
9. Eckart A. P., et. al., "Control of spectral transmission enhancement properties of random anti-reflecting surface structures fabricated using gold masking," Proc. SPIE 10115, Advanced Fabrication Technologies for Micro/Nano Optics and Photonics X, 101150B (2017).
10. Stolz, C. J., & Negres, R. A., “Ten-year summary of the Boulder Damage Symposium Annual Thin Film Laser Damage Competition,” Optical Engineering, 57(12), (2018).
11. Hobbs, Douglas S., Bruce D. MacLeod, and Juanita R. Riccobono. “Update on the Development of High-Performance Anti-Reflecting Surface Relief Micro-Structures.” *SPIE Proceedings,* April 27, 2007.
12. Ray, N. J., et. al., “Designer metasurfaces for antireflective applications enabled by Advanced Nanoparticle Technology,” Advanced Optical Materials, 10(10), (2022).
13. D. H. Raguin and G. M. Morris, "Antireflection structured surfaces for the infrared spectral region," Applied Optics, vol. 32, pp. 1154-1167, 1993/03/01 1993.
14. M. Ohring, The Materials Science of Thin Films. San Diego, California: Academic Press, 1992.

15. Thompson, Carl V. “Solid-State Dewetting of Thin Films.” *Annual Review of Materials Research* 42, no. 1 (August 4, 2012): 399–434.
16. Reiter, Günter. “Dewetting of Thin Polymer Films.” *Physical Review Letters* 68, no. 1 (January 6, 1992): 75–78.
17. Bischof, J., D. Scherer, S. Herminghaus, and P. Leiderer. “Dewetting Modes of Thin Metallic Films: Nucleation of Holes and Spinodal Dewetting.” *Physical Review Letters* 77, no. 8 (August 19, 1996): 1536–39.
18. Ray, N. J., et. al., “Substrate-engraved antireflective nanostructured surfaces for high-power laser applications," Optica 7, 518-526 (2020).
19. Ray, N. J., et. al., “Enhanced tunability of gold nanoparticle size, spacing, and shape for large-scale plasmonic arrays,” ACS Applied Nano Materials, 2(7), 4395–4401, (2019).
20. Herminghaus, Stephan, Karin Jacobs, Klaus Mecke, Jörg Bischof, Andreas Fery, Mohammed Ibn-Elhaj, and Stefan Schlagowski. “Spinodal Dewetting in Liquid Crystal and Liquid Metal Films.” *Science* 282, no. 5390 (October 30, 1998): 916–19.
21. Yadavali, Sagar, Mikhail Khenner, and Ramki Kalyanaraman. “Pulsed Laser Dewetting of AU Films: Experiments and Modeling of Nanoscale Behavior.” *Journal of Materials Research* 28, no. 13 (May 14, 2013): 1715–23.
22. Cardinaud, Christophe, Marie-Claude Peignon, and Pierre-Yves Tessier. “Plasma Etching: Principles, Mechanisms, Application to Micro- and Nano-Technologies.” *Applied Surface Science* 164, no. 1–4 (September 2000): 72–83.
23. Economou, Demetre J. “Modeling and Simulation of Plasma Etching Reactors for Microelectronics.” *Thin Solid Films* 365, no. 2 (April 2000): 348–67.
24. Hobbs, Douglas S., and Bruce D. MacLeod. “Design, Fabrication, and Measured Performance of Anti-Reflecting Surface Textures in Infrared Transmitting Materials.” *SPIE Proceedings* 5786 (May 18, 2005): 349.
25. Zollars, Byron, Steve Savoy, Qizhen Xue, Jeremy John, Kyle Hoover, Gabriel Elpers, and Roger Wood. “Performance Measurements of Infrared Windows with Surface Structures Providing Broadband Wide-Angle Antireflective Properties.” *SPIE Proceedings* 8708 (June 4, 2013).
26. Wilson, Christopher R., Thomas C. Hutchens, Jesse A. Frantz, Lynda E. Busse, L. Brandon Shaw, Jasbinder S. Sanghera, and Ishwar D. Aggarwal. “Laser Damage Testing of Windows with Anti-Reflection Structured Surfaces for High Power Continuous-Wave near-Infrared Laser Applications.” *Window and Dome Technologies and Materials XVI*, May 17, 2019, 13.
27. Wilson, C. R., et. al., “Laser damage of silica optical windows with random antireflective structured surfaces,” Opt. Eng. 57(12), 121906 (2018).
28. Busse, L. E. et al., "Ultrashort Pulse Laser Irradiation Tests on Silica Glass with Random Antireflective Surface Structures," Conference on Lasers and Electro-Optics (CLEO), pp. 1-2 (2018).
29. Weber, Marvin. “Handbook of Optical Materials.” *Laser & Optical Science & Technology*, September 24, 2002.
30. Moore, Lisa A., and Charlene M. Smith. “Fused Silica as an Optical Material [Invited].” *Optical Materials Express* 12, no. 8 (July 15, 2022): 3043.

31. Assael, M. J., S. Botsios, K. Gialou, and I. N. Metaxa. “Thermal Conductivity of Polymethyl Methacrylate (PMMA) and Borosilicate Crown Glass BK7.” *International Journal of Thermophysics* 26, no. 5 (September 2005): 1595–1605
32. Seungmuk, J., et al. “Improved antireflection properties of moth eye mimicking nanopillars on transparent glass: Flat antireflection and color tuning,” Nanoscale, 4(15), 4603-4610, (2012).
33. O. S. Heavens, Optical properties of thin solid films. New York: Dover Publications, 1991.

APPENDIX A: PUBLICATIONS AND CONFERENCE PROCEEDINGS

Vaca, Benjamin A., Jude K. Yoshino, Tyler A. Benge, William E. Genet, Ishwar D. Aggarwal, and Thomas C. Hutchens. "Transmission Enhancement via Metasurfaces with Tunable Waveband Performance by Dewetting and Seeded Masking." *Advanced Optics for Imaging Applications: UV through LWIR IX,* June 7, 2024, 4.

Vaca, Benjamin A., Jude K. Yoshino, William E. Genet, Tyler A. Benge, Ishwar D. Aggarwal, and Thomas C. Hutchens. "Incremental Plasma Etching and Depletion of Metal Mask for Generating ARSS on Fused Silica Optical Windows." *CLEO 2024,* 2024.

Vaca, Benjamin A., Jude K. Yoshino, William E. Genet, Tyler A. Benge, Ishwar D. Aggarwal, and Thomas C. Hutchens. "Metal Etch Mask Morphology for Silica Optical Windows Verified by Transmission Spectra." *CLEO 2024*, 2024.

APPENDIX B: METAL MASK DATABASE

Table 5: List of Metallic Etch Masks

Mask Label	Deposition Metal, Thickness (nm)	Annealing Temperature (C)	Rounds
5nmAu-300C	Gold, 5	300	1
5nmAu-400C	Gold, 5	400	1
5nmAu-500C	Gold, 5	500	1
5nmAu-300CR2	Gold, 5	300	2
5nmAu-400CR2	Gold, 5	400	2
5nmAu-500CR2	Gold, 5	500	2
5nmAu-300CR3	Gold, 5	300	3
5nmAu-400CR3	Gold, 5	400	3
5nmAu-500CR3	Gold, 5	500	3
5nmAu-300CR4	Gold, 5	300	4
5nmAu-400CR4	Gold, 5	400	4
5nmAu-500CR4	Gold, 5	500	4
10nmAu-300C	Gold, 10	300	1
10nmAu-400C	Gold, 10	400	1
10nmAu-500C	Gold, 10	500	1
10nmAu-300CR2	Gold, 10	300	2
10nmAu-400CR2	Gold, 10	400	2
10nmAu-500CR2	Gold, 10	500	2
10nmAu-300CR3	Gold, 10	300	3
10nmAu-400CR3	Gold, 10	400	3
10nmAu-500CR3	Gold, 10	500	3
10nmAu-300CR4	Gold, 10	300	4
10nmAu-400CR4	Gold, 10	400	4
10nmAu-500CR4	Gold, 10	500	4
15nmAu-300C	Gold, 15	300	1
15nmAu-400C	Gold, 15	400	1
15nmAu-500C	Gold, 15	500	1
15nmAu-300CR2	Gold, 15	300	2
15nmAu-400CR2	Gold, 15	400	2
15nmAu-500CR2	Gold, 15	500	2
15nmAu-300CR3	Gold, 15	300	3
15nmAu-400CR3	Gold, 15	400	3
15nmAu-500CR3	Gold, 15	500	3

15nmAu-300CR4	Gold, 15	300	4
15nmAu-400CR4	Gold, 15	400	4
15nmAu-500CR4	Gold, 15	500	4
5nmAg-300C	Silver, 5	300	1
5nmAg-400C	Silver, 5	400	1
5nmAg-500C	Silver, 5	500	1
10nmAg-300C	Silver, 10	300	1
10nmAg-400C	Silver, 10	400	1
10nmAg-500C	Silver, 10	500	1
15nmAg-300C	Silver, 15	300	1
15nmAg-400C	Silver, 15	400	1
15nmAg-500C	Silver, 15	500	1
5nmPt-800C	Platinum, 5	800	1
5nmPt-900C	Platinum, 5	900	1
10nmPt-800C	Platinum, 10	800	1
10nmPt-900C	Platinum, 10	900	1
15nmPt-800C	Platinum, 15	800	1
15nmPt-900C	Platinum, 15	900	1

SEMs for repetitive Au masking

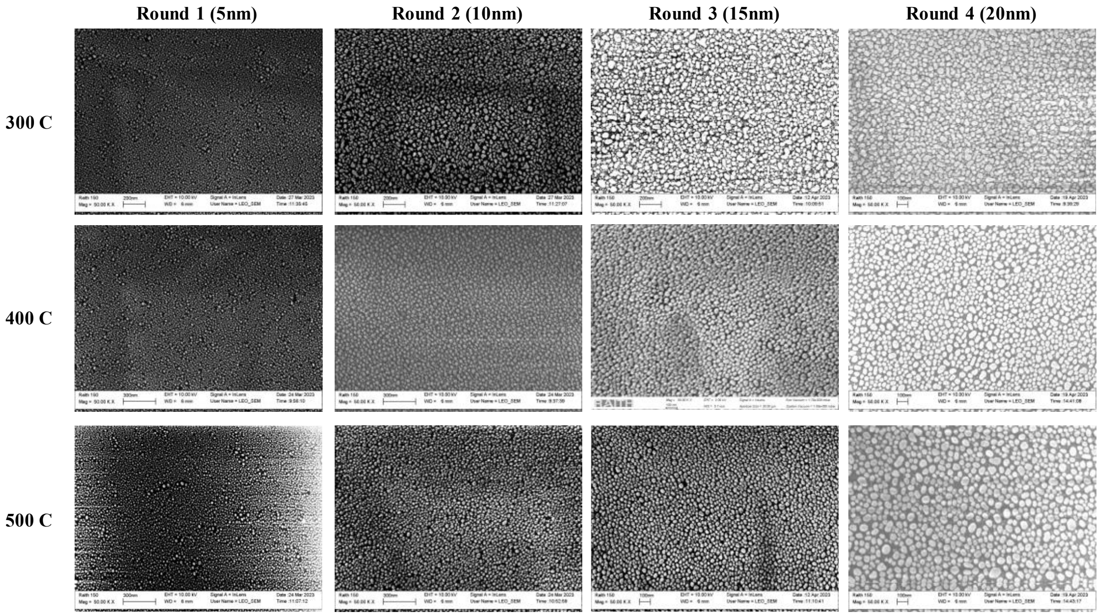

Figure 42: SEM images of repetitive Au masking for 4 rounds of 5 nm Au deposition followed by annealing at 300, 400, and 500 °C. Images were taken at 50,000x magnification.

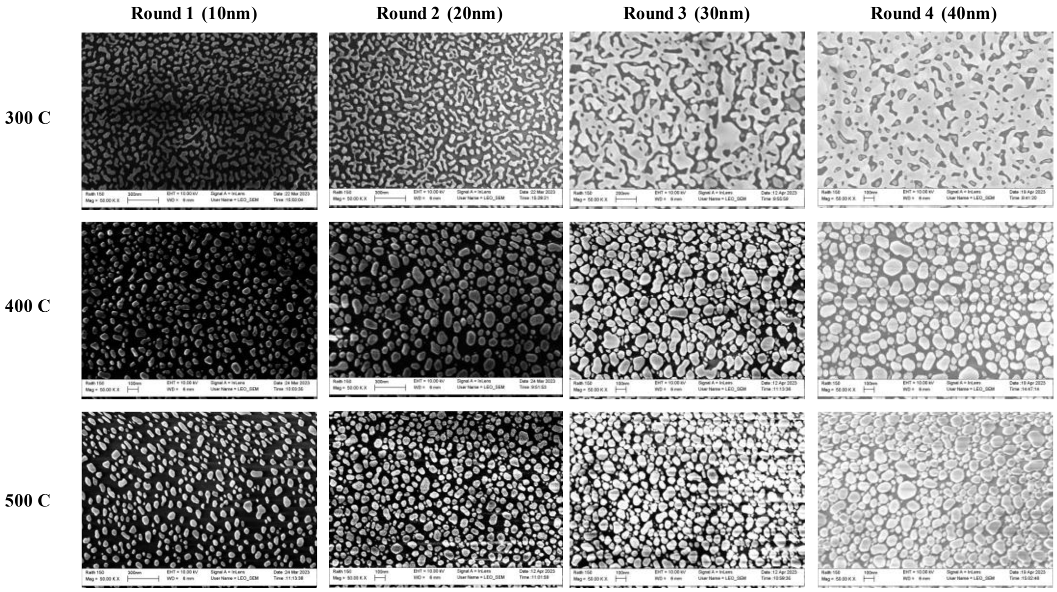

Figure 43: SEM images of repetitive Au masking for 4 rounds of 10 nm Au deposition followed by annealing at 300, 400, and 500 °C. Images were taken at 50,000x magnification.

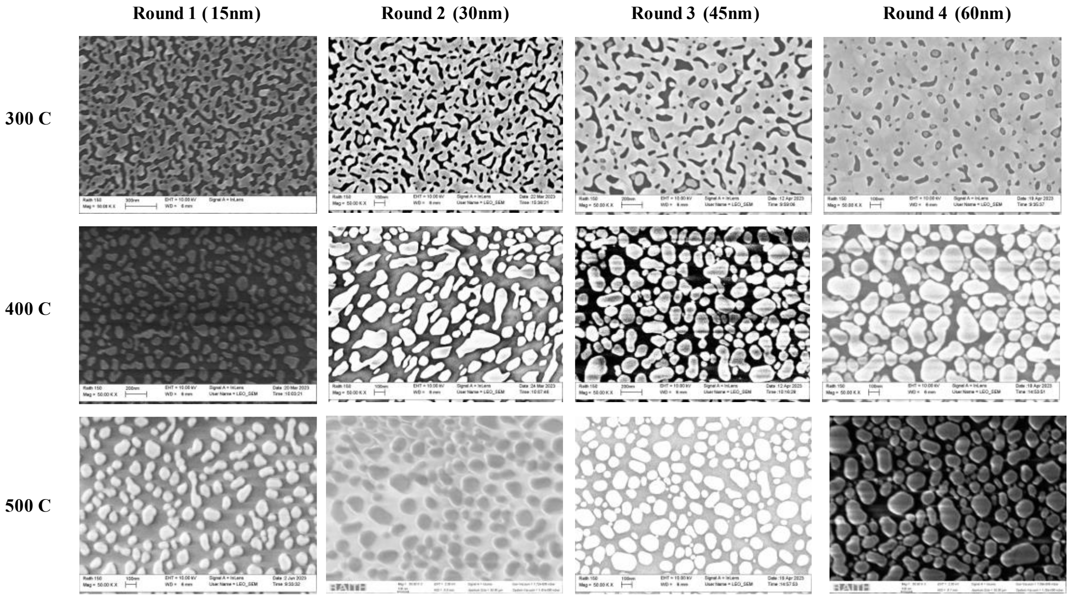

Figure 44: SEM images of repetitive Au masking for 4 rounds of 15 nm Au deposition followed by annealing at 300, 400, and 500 °C. Images were taken at 50,000x magnification.

SEM images at 45° AOI for ARSS resulting from each metal mask

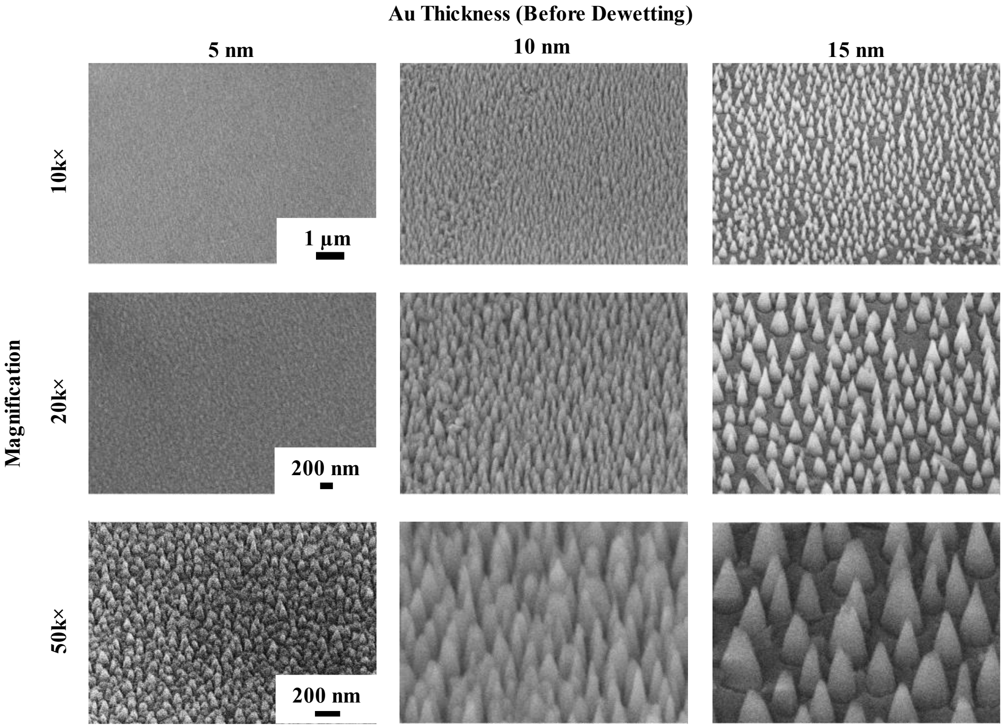

Figure 45: SEM images of the resulting ARSS after etching three initial Au deposition thicknesses 5, 10 and 15 nm until metal mask depletion. Images were taken at 10,000x, 20,000x, and 50,000x magnification at 45° AOI.

SEM feature analysis for each metal mask tested

Table 6: SEM Image Analysis for Au Masking (Single Round)

Deposition Thickness (nm)	Annealing Temperature (C)	Average Equivalent Dia. (nm)	Average Periodicity (nm)
5	300	19	55
	400	34	69
	500	31	115
10	300	51	103
	400	54	106
	500	59	122
15	300	43	77
	400	87	172
	500	88	177

Table 7: SEM Image Analysis for Pt Masking (Single Round)

Deposition Thickness (nm)	Annealing Temperature (C)	Average Equivalent Dia. (nm)	Average Periodicity (nm)
5	800	56	152
	900	50	131
10	800	43	115
	900	56	109
15	800	48	88
	900	62	105

Table 8: SEM Image Analysis for Ag Masking (Single Round)

Deposition Thickness (nm)	Annealing Temperature (C)	Average Equivalent Dia. (nm)	Average Periodicity (nm)
5	300	13	46
	400	15	47
	500	12	43
10	300	23	76
	400	49	91
	500	49	94
15	300	Na	Na
	400	72	133
	500	101	178

APPENDIX C: SUBSTRATES, EQUIPMENT, AND PROCESSES USED

Table 9: List of Substrates

Substrate Name	Diameter, Thickness (in)
Edmund 7979 Fused Silica	1, 0.03937
Edmund 7979 Fused Silica	1, 0.11811
ESCO 7980 Fused Silica	1, 0.09375
Quartz Plus Inc. 7980 Fused Silica	1, 0.0625
JGS2 Fused Silica Wafer	NA, 0.01968
BK7 Borosilicate	1, 0.03937
Edmund JGS2 Fused Silica	8, 1.5

Table 10: List of Equipment for Fabrication and Analysis

Equipment Name	Application for Fabrication/Analysis
AJA Sputtering Tool	Metal Thin Film Deposition
Lesker E-Beam Evaporation Machine	Metal Thin Film Deposition
Nabertherm Furnace (Small and Large	Annealing, Dewetting
Raith 150 SEM	Feature Analysis
LEXT Olympus Microscope	Feature Analysis
CARY Spectrometer	Spectra Analysis
J.A. Woollam RC2 Ellipsometer	Spectra Analysis
PlasmaTherm 7000	Plasma Etching
MATLAB	Feature Analysis
EXCEL	Feature/Spectra Analysis
Gantry	Uniformity Analysis

MATLAB codes

SEM Image Analysis:

```
% Read the binary image
Image = imread('60s500CR4 65min_Binary.JPG'); % Replace 'your_image.jpg' with
the actual image filename
binaryImage = im2bw(Image);
```

```
% Calculate the fill factor
fill=0;
for N = 1:1000
    for M = 1:500
        if Image(M,N)<=120 %Set the threshold value between 0 and 255
            c(M,N)=0;
        else
            c(M,N)=255;
            fill=fill+1;
        end
    end
end

fillFactor=fill/500000 %Output the fill factor percentage of the total array
area


%Calculate Separation Distance
connectedComponents = bwconncomp(binaryImage);  % Label connected components
in the binary image

Centers = regionprops(binaryImage,{'Centroid'},{'Area'});
CentersTable = struct2table(Centers);
PreCentersArray = table2array(CentersTable);
Blobs = regionprops(binaryImage,{'Area'});
BlobsTable = struct2table(Blobs);
BlobsArray = table2array(BlobsTable);
TooSmall = find(BlobsArray<4);
PreCentersArray(TooSmall,:) = NaN;
NewCentersX = PreCentersArray(:,1);
NewCentersX2 = NewCentersX(~isnan(NewCentersX));
NewCentersY = PreCentersArray(:,2);
NewCentersY2 = NewCentersY(~isnan(NewCentersY));
CentersArray = [NewCentersX2,NewCentersY2];
% histogram(BlobsArray,'BinWidth',1)


numObj = numel(NewCentersX2);
ShortestDistanceArray = zeros(numObj,2);

for n = 1 : numObj
    CentersArray(n,:) = NaN;
    CentersX = CentersArray(:,1);
    CentersX2 = CentersX(~isnan(CentersX));
    CentersY = CentersArray(:,2);
    CentersY2 = CentersY(~isnan(CentersY));
    CentersArray2 = [CentersX2,CentersY2];
    CentersArray = [NewCentersX2,NewCentersY2];
    [k,dist] = dsearchn(CentersArray2,CentersArray(n,:));
    ShortestDistanceArray(n,:) = [n,dist];

end
ShortestDistanceMean = mean(ShortestDistanceArray(:,2));
disp('Shortest Mean =')
disp(ShortestDistanceMean)
```

```
RadialMeanArray=zeros(numObj,2);
RadiusSetting=2;

imshow(Image)
hold on

for n = 1 : numObj
    plot(CentersArray(n,1),CentersArray(n,2),'r*')
    CentersArray(n,:) = NaN;
    CentersX = CentersArray(:,1);
    CentersX2 = CentersX(~isnan(CentersX));
    CentersY = CentersArray(:,2);
    CentersY2 = CentersY(~isnan(CentersY));
    CentersArray2 = [CentersX2,CentersY2];
    CentersArray = [NewCentersX2,NewCentersY2];
    [Idx,Distance] = knnsearch(CentersArray2,CentersArray(n,:),"K",15);
    BeyondRadius=find(Distance>ShortestDistanceMean*RadiusSetting);
    Distance(BeyondRadius) = NaN;
    if isnan(Distance(1))
        [Idx,Distance] = knnsearch(CentersArray2,CentersArray(n,:),"K",1);
    end
    Distance2 = Distance(~isnan(Distance));
    MeanWithinRadius = mean(Distance2);
    RadialMeanArray(n,:) = [n,MeanWithinRadius];
end

RadialMean=mean(RadialMeanArray(:,2));

disp('Radial Mean =')
disp(RadialMean)


% Calculate the connected components in the binary image
cc = bwconncomp(binaryImage);

% Calculate the average size of objects
objectSizes = cellfun(@numel, cc.PixelIdxList);
averageSize = mean(objectSizes);

% Display the results
disp(['Fill factor: ', num2str(fillFactor)]);

disp(['Average size: ', num2str(averageSize)]);

disp(['Radia Mean Separation Distance: ', num2str(RadialMean)]);
```

Uniformity Scan Analysis:

```
%% Data Manipulation 1
data = readmatrix('8inc_JGS2_1064_ARSS.csv');
pad = 4;
```

```
dataPad = zeros(101,101+2*pad);
M = max(data,[],'all')
datanorm = data/M;
%datalog= log(1+datanorm);
%M = max(datalog,[],'all')
%datalognorm = datalog/M;

%% Flip Data
c = zeros(101,101);
c(1:40,:) = -1;
c(72:end,:) = 2;
for k = 1:2:length(data)
    datanorm(k,:) = flip(datanorm(k,:));
end


%center = datanorm(round(length(data)/2),:);

%% Center Avg
centerWidth = 5; % Must be odd
center = datanorm(round(length(data)/2),:);
n=1
for k = 1:1:floor(centerWidth/2)
    center = center + datanorm(round(length(data)/2+k),:);
    center = center+ datanorm(round(length(data)/2-k),:);
    n=n+1
end
center = center/centerWidth;


%% Figure
hfig = figure(3);
tiledlayout(1,2);

%%%%%%%%%%%%%%%%%%%%%%%%%%%%%%%%%%%%%%%%%%%%%%%%%%%%%%%%%%%%%%%%%%%%%%%%%%%%%%%%%
nexttile;
imagesc(datanorm,'CDataMapping','scaled')
cb = colorbar;
colormap("Pink");
title("532nm Transmission of JGS2 8in Dia. by 2in Thick Blank",'FontName',
'Times New Roman', 'FontSize', 25)
xlabel("(mm)",'FontName', 'Times New Roman', 'FontSize', 25)
ylabel("(mm)",'FontName', 'Times New Roman', 'FontSize', 25)
axis square;
grid on;

%% Color Bar Range
clim([0.85 1]);



distance_between_points = 2; % in mm

% Define desired tick interval (for example, every 20mm)
tick_interval_mm = 20; % in mm
```

```
tick_interval_points = tick_interval_mm / distance_between_points;

% Define tick positions
x_ticks = 0:tick_interval_points:(size(dataPad, 2) - 1);
y_ticks = 0:tick_interval_points:(size(dataPad, 1) - 1);

% Set the tick marks on the x and y axes
set(gca, 'XTick', x_ticks, 'YTick', y_ticks);

% Set the tick labels to reflect the distances
x_tick_labels = arrayfun(@(x) sprintf('%.0f', x * distance_between_points),
x_ticks, 'UniformOutput', false);
y_tick_labels = arrayfun(@(y) sprintf('%.0f', y * distance_between_points),
y_ticks, 'UniformOutput', false);

set(gca, 'XTickLabel', x_tick_labels, 'YTickLabel', y_tick_labels, 'FontName',
'Times New Roman', 'FontSize', 25);

%%%%%%%%%%%%%%%%%%%%%%%%%%%%%%%%%%%%%%%%%%%%%%%%%%%%%%%%%%%%%%%%%%%%%%%%%%%
nexttile;


plot(center)

title(" Cross Section Transmission of JGS2 8in Dia. by 2in Thick ARSS
SS",'FontName', 'Times New Roman', 'FontSize', 12)
xlabel("(mm)",'FontName', 'Times New Roman', 'FontSize', 12)
ylabel("(Normalized % Transmission)",'FontName', 'Times New Roman',
'FontSize', 12 );
ylim([0.9 1])
axis square;
grid on;


%Define tick interval
tick_interval_mm = 20; % in mm
tick_interval_points = tick_interval_mm / distance_between_points;


% Define tick positions
x_ticks = 0:tick_interval_points:(size(center, 2) - 1);
y_ticks = 0:.01:1;
% Set the tick marks on the x and y axes
set(gca, 'XTick', x_ticks, 'YTick', y_ticks);

% Set the tick labels to reflect the distances
x_tick_labels = arrayfun(@(x) sprintf('%.0f', x * distance_between_points),
x_ticks, 'UniformOutput', false);

set(gca, 'XTickLabel', x_tick_labels );
```